

The Phase Separation Inlet for Droplets, Ice Residuals, and Interstitial Aerosols

by

Libby Koolik

B.S. Earth, Atmospheric, and Planetary Sciences
Massachusetts Institute of Technology, 2017

Submitted to the
Department of Civil and Environmental Engineering
in Partial Fulfillment of the Requirements for the Degree of

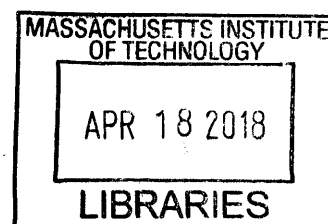
Master of Engineering

at the

Massachusetts Institute of Technology

February 2018

© 2018 Koolik
All rights reserved



ARCHIVES

The author hereby grants to MIT permission to reproduce and to distribute
publicly paper and electronic copies of this thesis document in whole or in part in
any medium now known or hereafter created.

Signature of Author _____

Signature redacted

Department of Civil and Environmental Engineering
January 1, 2017

Certified by _____

Signature redacted

/ Daniel Cziczo
Associate Professor of Atmospheric Chemistry
Thesis Supervisor

Accepted by _____

Signature redacted

/ Jesse Kroll
Professor of Civil and Environmental Engineering
Chair, Graduate Program Committee

The Phase Separation Inlet for Droplets, Ice Residuals, and Interstitial Aerosols

by
Libby Koolik

Submitted to the Department of Civil and Environmental Engineering on January 1, 2017, in
partial fulfillment of the requirements for the degree of
Master of Engineering

Abstract

A new inlet for studying the composition of mixed-phase clouds – the phaSe seParation Inlet for Droplets icE residuals and inteRstitial aerosols (SPIDER) – is described. SPIDER combines an omni-directional inlet, a Large-Pumped Counterflow Virtual Impactor (L-PCVI), a flow tube as evaporation chamber, and a Pumped Counterflow Virtual Impactor (PCVI) to separate droplets, ice crystals, and interstitial aerosols for simultaneous sampling. Verification tests of each individual component of SPIDER were positive, as was the result of investigating that the components work together as a whole setup without flow blockage or choking. SPIDER was installed at Mt. Washington Observatory (MWO), a mountain top research facility in the White Mountains, for a two-week field campaign. There, SPIDER showed promising performance as a field instrument and provided first data that suggest its capability of separating distinct cloud particles. Future design improvements of SPIDER are suggested along with potential locations for field measurements.

Thesis Supervisor: Daniel Cziczo

Title: Associate Professor of Atmospheric Chemistry

Table of Contents

- 0. Title Page
- 1. Abstract
- 2. Introduction and Literature Review
 - 2.1. Motivation
 - 2.2. Current Understanding of Mixed-Phase Clouds
- 3. Methodology
 - 3.1. Mixed-Phase Cloud Sampling Technology
 - 3.1.1. Overview of Instruments
 - 3.1.2. Counterflow Virtual Impactors
 - 3.1.3. Cloud Phase Separation Devices
 - 3.2. 3D Printing Techniques
 - 3.2.1. Additive Manufacturing Overview
 - 3.2.2. Stereolithography Apparatus Printing
 - 3.3. Phase Separation Inlet
- 4. Design and Development of Cloud Phase Separation Inlet
 - 4.1. Theory of Operation
 - 4.2. Design and Construction
 - 4.2.1. Computer Aided Design Using Solidworks
 - 4.2.2. 3D Printing Using Formlabs Form2
 - 4.2.3. Mechanical Construction
 - 4.3. Incorporated Commercial Instrumentation
 - 4.3.1. Optical Particle Sizer
 - 4.3.2. Optical Particle Counter
 - 4.3.3. Mass Flow Controllers
 - 4.3.4. Low Temperature Cooling Bath
 - 4.3.5. Temperature Sensors
- 5. Verification Experiments
 - 5.1. Large Pumped Counterflow Virtual Impactor (L-PCVI) Cut-off Measurements
 - 5.1.1. Lower Bound of the L-PCVI Experiment
 - 5.1.2. L-PCVI Verification Test
 - 5.1.3. Summary of L-PCVI Results
 - 5.2. Flow Chamber Temperature Calibration and Response Measurements
 - 5.2.1. Temperature Sensor Calibration
 - 5.2.2. Chamber Response Calibration
 - 5.3. Flow Chamber Verification
 - 5.3.1. Droplet Evaporation Modeling
 - 5.3.2. Maintaining Ice Crystals
 - 5.4. Pumped Counterflow Virtual Impactor (PCVI) Cut-off Measurements
 - 5.4.1. Experimental Setup
 - 5.4.2. Results and Discussion
 - 5.4.3. Summary of PCVI Results

- 5.5. Flow Verification
- 6. Mt. Washington Observatory Field Campaign
 - 6.1. Mount Washington Observatory Field Site
 - 6.2. Durability and Deployability
 - 6.2.1. Transportation
 - 6.2.2. Deployment
 - 6.3. Sample Verification Measurements
- 7. Summary and Future Work
 - 7.1. Analysis of Performance
 - 7.2. Future Improvements
 - 7.3. Future Field Studies
 - 7.4. Conclusions
- 8. Acknowledgements
- 9. References
- 10. Tables
- 11. Figures
- 12. CAD Drawings

List of Abbreviations

3D	Three-dimensional
AF	Add Flow
AM	Additive Manufacturing
CAD	Computer-Aided Design
CCN	Cloud Condensation Nucleus
CFD	Computational Fluid Dynamics
CLH	Closed-Path Tunable Diode Laser Hygrometer
CPI	Cloud Particle Imager
CSI	Cloud Spectrometer and Imager
CVI	Counterflow Virtual Impactor
D50	50% Transmission Cut Size
ECF	Effective Counterflow
FDM	Fused Deposition Modeling
Ice-CVI	Ice-Counterflow Virtual Impactor
IF	Input Flow
IKP-2	Isokinetic Total Water Content Evaporator
INP	Ice Nucleating Particle
IPA	Isopropyl Alcohol
ISI	Ice Selective Inlet
IS-PCVI	Ice-Selecting PCVI
IWC	Ice Water Content
LOM	Laminated Object Manufacturing
L-PCVI	Large-Pumped Counterflow Virtual Impactor
LWC	Liquid Water Content
MFC	Mass Flow Controller
MWO	Mount Washington Observatory
OPC	Optical Particle Counter
OPS	Optical Particle Sizer
PCVI	Pumped Counterflow Virtual Impactor
PF	Pump Flow
SF	Sample Flow
SLA	Stereolithography Apparatus
SLS	Selective Laser Sintering
SOA	Secondary Organic Aerosol
SPIDER	phaSe seParation Inlet for Droplets, icE residuals, and inteRstitial aerosols
STL	Standard Tessellation Language
TWC	Total Water Content
WBF	Wegener-Bergeron Findeisen

2. Introduction and Literature Review

Mixed phase clouds contain two distinct water phases simultaneously. “Mixed-phase” is an umbrella term that captures a wide range of clouds because no specific definition currently exists (Shupe et al., 2006). Rather, according to Korolev et al. (2003), a cloud is considered “mixed-phase” so long as both liquid and ice phase are present within the cloud. For clouds in this group, the ratio of liquid to solid water particles can vary as well as the height and location in the atmosphere. These clouds are generally associated with low-level stratiform Arctic clouds, yet they are known to occur worldwide and year-round (Shupe et al., 2008).

There is currently a global effort to study these clouds in order to refine the definition of what it means to be a mixed-phase cloud and the effects they have on climate and aviation (Abel et al., 2014; Davis et al., 2007a; Hiranuma et al., 2016b; Kupiszewski et al., 2015; Mertes et al., 2007; Patade et al., 2015). I will now present the motivation behind studying mixed-phase clouds and then discuss the current understanding of their structure and composition.

2.1. Motivation

Mixed-phase clouds are important because they pose both a physical problem in aviation and a scientific problem in climate. In aviation, mixed-phase clouds are a significant threat for aircrafts when the ratio of liquid to water is unknown. These clouds are known to cause aircraft icing from super-cooled droplets, and excessive icing can result in engine power loss (Shupe et al., 2008; Strapp et al., 2016).

In climate, all clouds play a significant role in the earth’s radiative budget, yet the extent to which they warm or cool the planet is greatly uncertain (Boucher et al., 2013). Clouds interact with incoming radiation in both the cloud albedo effect and the cloud lifetime effect. The cloud albedo effect describes changes to the radiative forcing at the top of the atmosphere which occur due to an increase in cloud spatial and temporal extent as a result of increasing aerosol from industrialization. The lifetime effect refers to the decreased lifetime of a cloud due to an increased amount of aerosols causing smaller cloud droplets and less efficient precipitation (Lohmann and Hoose, 2009; Storelvmo et al., 2008). Mixed-phase clouds are complicated because the partitioning of liquid and solid phase water is critical in assessing these effects for a given cloud. At present, these effects are difficult to parameterize in models because of an overall lack of observational research on formation, microphysical properties, and phase partitioning (Kamphus et al., 2010; Shupe et al., 2006).

Understanding the composition of mixed-phase clouds is critical for reducing uncertainty in climate modeling. The ratio of water droplets to ice crystals greatly affects properties of clouds important for understanding their interaction with radiation: cloud extent, cloud lifetime, and precipitation efficiency (Atkinson et al., 2013; Hirst et al., 2001; Korolev et al., 2003; Shupe et al., 2006). These differences arise because ice crystals and water droplets vary in size, shape, and refractive properties (Shupe et al., 2006). Estimations of partitioning can lead to significant discrepancies in models because of these differences. With higher proportions of liquid droplets, for example, there will be a stronger planetary albedo in the model because droplets are more reflective (McCoy et al., 2016). Conversely, higher proportions of ice crystals results in enhanced precipitation (Tsushima et al., 2006; Verheggen et al., 2007). Just understanding how prevalent mixed phase clouds are can have a significant effect on models; the presence of two phases leads to longer-living clouds, for example (Atkinson et al., 2013; Verlinde et al., 2007).

The stalemate in political action combating climate change is often attributed to the scientific uncertainty in the climate system (Boucher et al., 2013; Kupiszewski et al., 2015). Specifically, many members of the climate change community cite mixed-phase clouds as a key parameter to reduce uncertainty in future climate models (Boucher et al., 2013; McCoy et al., 2016; Shupe et al., 2006; Storelvmo et al., 2008; Verlinde et al., 2007; Wang et al., 2012). The IPCC estimates the effective radiative forcing from greenhouse gases as between 2.26 to 3.40 W/m², yet the contribution from aerosols and clouds ranges from -1.2 to 0.0 W/m² (Myhre et al., 2013). This uncertainty is much higher and spans from cooling agent to having no effect. Thus, it is critical that more research is done to minimize scientific uncertainty in the role of mixed-phase clouds on the overall climate system.

2.2. Current Understanding of Mixed-Phase Clouds

The individual microphysical formation processes of water and ice clouds are relatively well understood. Water droplets form as a result of the Köhler effect: as particles known as cloud condensation nuclei (CCN) reach critical supersaturation, they activate to form droplets (Lohmann and Hoose, 2009; Wang et al., 2012). Ice nucleation is more complex. Ice can form homogeneously at temperatures below roughly -40°C (Atkinson et al., 2013; Kamphus et al., 2010; Korolev et al., 2003; Storelvmo et al., 2008; Verheggen et al., 2007; Wang et al., 2012). At higher temperatures, ice forms heterogeneously through a number of different pathways using ice nucleating particles (INPs) (Atkinson et al., 2013; Kamphus et al., 2010; Lohmann and Hoose, 2009; Storelvmo et al., 2008; Tsushima et al., 2006; Verheggen et al., 2007; Wang et al., 2012). Specific microphysical and chemical properties of INPs that result in strong ice nucleation are still poorly understood (Shupe et al., 2008), though it is widely accepted that mineral dusts are efficient INPs (Kamphus et al., 2010; Wang et al., 2012).

Recent studies have helped the scientific community to better understand the properties of effective INPs, and this could lead to a better understanding of mixed-phase cloud partitioning. I will now summarize a few examples of recent findings in the field:

Two recent publications provide examples of laboratory investigations into the efficiency of INPs specifically relevant for mixed-phase clouds. By performing studies using droplet freezing techniques and optical microscopy, Atkinson et al. (2013) showed the INP activation of many minerals and found that increased feldspar content in a particle increases the freezing temperature of droplets to 50% activation temperature of 250.5 K (Atkinson et al., 2013). This is important, given the high crustal abundance of feldspars. By generating secondary organic aerosol (SOA) particles of varying oxygen-to-carbon ratios and subjecting them to an ice nucleation chamber and microscopy, Wang et al. (2012) found that SOA particles act as INPs at temperatures between 230 and 245 K, which is within range of the homogeneous nucleation temperature (Wang et al., 2012). From these results, the authors argue that SOA coatings need to be considered in future atmospheric models as they significantly reduce efficiency of INPs (Wang et al., 2012).

While laboratory measurements are helpful, in-situ observations are required to understand the natural efficiency of INP and microphysics of mixed-phase clouds. Many of these experiments have occurred in the Arctic due to the prevalence of mixed-phase stratiform clouds (41% of the time (Shupe et al., 2006)) and the strong effect of climate change on the Arctic (estimated to be warming approximately twice as fast as the global average (Verlinde et al., 2007)). Another common research location is Jungfraujoch, a research base in Switzerland.

Jungfraujoch is popular for its cloud coverage (37% of the time) and the prevalence of mixed-phase clouds (Kamphus et al., 2010; Verheggen et al., 2007).

Korolev et al. (2003) performed a detailed study of frontal systems and their associated mixed-phase clouds from five field campaigns (two Arctic) using the Nevzorov probe, which samples liquid water content (LWC) and total ice and liquid water content (TWC) and will be described in more detail in Section 3.1.1. (Korolev et al., 2003). Ultimately, they found that mixed-phase cloud occurrence is relatively constant with temperature, yet there is a slight decrease in ice water content (IWC) as temperature decreases (Korolev et al., 2003). This is counter-intuitive, yet could be attributed to low INP concentrations or riming.

Shupe et al. (2005) discussed cloud properties observed during a 12-month field campaign in the Arctic. There is consensus among scientists that naturally-occurring stratiform Arctic mixed-phase clouds have layers of ice sheets topped by water (Korolev et al., 2003; Shupe et al., 2006; Verlinde et al., 2007). This study confirmed this while adding that this phenomenon is not seasonally dependent (Shupe et al., 2006). They also observed substantial differences between mixed-phase and pure-ice clouds in the Arctic with respect to ice properties and vertical distribution of particles (Shupe et al., 2006). This suggests that there are different growth and formation mechanisms responsible and that the presence of water is fundamental in the formation of ice in mixed-phase clouds.

Verlinde et al. (2007) described a 25-day field campaign in which they collected information about cloud microphysics, radiative properties, and thermodynamics of mixed-phase Arctic clouds (Verlinde et al., 2007). They described the three cases studied: a single-layer stratocumulus cloud at the boundary level, a cirrus cloud, and a multilayer stratus cloud. There was a high amount of sensitivity regarding changes in atmospheric dynamics and cloud characteristics (Verlinde et al., 2007). One key result of their investigation was that the layers of the mixed-phase clouds can be characterized as having ice precipitation shafts separating the distinct liquid layers (Verlinde et al., 2007).

Verheggen et al. (2007) used probes to analyze aerosol partitioning in mixed-phase clouds during three campaigns at Jungfraujoch (Verheggen et al., 2007). They found that the fraction of activated CCN is consistent with Köhler theory and increases with increasing particle size, with a few exceptions attributed to external mixing of soluble with insoluble aerosols (Verheggen et al., 2007). They described the activated fraction as dependent on availability of water vapor, air updraft velocity, CCN and INP number concentration, and large-scale dynamics, specifically indicating number concentration of INP as the limiting factor in ice formation (Verheggen et al., 2007). This study confirms many aforementioned results.

Kamphus et al. (2010) performed two month-long particle mass spectrometry campaigns at Jungfraujoch using the Ice-Counterflow Virtual Impactor (Ice-CVI) (Kamphus et al., 2010), which will be detailed more thoroughly in Section 3.1.1. They found that in all mixed-phase clouds sampled, droplets outnumbered ice crystals by two orders of magnitude. Additionally, Kamphus et al. (2010) compared INP and CCN composition, finding that CCN predominantly contain sulfates and nitrates while INPs are devoid of these (Kamphus et al., 2010). The concentration of mineral dust is low in background concentrations while high in INP concentrations (Kamphus et al., 2010). This further indicates the importance of mineral dust in ice nucleation.

There is still uncertainty in the specific combination of properties that constitute an effective INP in the natural formation of ice crystals. One question is how both phases of water can co-exist in the same environment? The most accepted answer to this problem is known as the

Wegener-Bergeron-Findeisen (WBF) process, which is known to play a role in the formation of mixed-phase clouds. WBF process refers to the phenomenon whereby ice crystals grow at the expense of droplet shrinkage due to thermodynamic instability (Korolev, 2007; Pruppacher and Klett, 1997). Ice crystals have a lower saturation vapor pressure than the water droplets that exist nearby; as a result, the crystals will grow and nucleate at a faster rate, lowering the relative humidity and causing the droplets to shrink or evaporate altogether (Shupe et al., 2006; Storelvmo et al., 2008; Tsushima et al., 2006; Verheggen et al., 2007). This effect is limited by the availability of INPs in the cloud, since INPs are less common among ambient aerosols than CCNs and WBF requires vapor to freeze heterogeneously on the surface of INPs (Verheggen et al., 2007). There is some skepticism surrounding WBF: while Verheggen et al. (2007) showed that observations of aerosol partitioning are consistent with WBF (Verheggen et al., 2007), Korolev (2007) demonstrated that WBF has its limitations and does not occur under all conditions in mixed-phase clouds. Sufficient updraft velocity can cause simultaneous growth of droplets and crystals while sufficient downdraft velocity can cause simultaneous evaporation (Korolev, 2007).

While WBF has been described physically by numerous scientists, climate modelers are still working to capture the exact effect of the phenomenon. Lohmann and Hoose (2009) varied the WBF and sulfate-coating parameters to study the effects on radiative effects of mixed-phase clouds. They found that including WBF increased the radiative effect of the glaciation effect (reduction in cloud cover by the uptake of water vapor by ice) by 0.12 to 0.20 W/m², depending on treatment of the WBF process (Lohmann and Hoose, 2009). When combining the effects of WBF and sulfate-coatings, the simulation yielded 0.47 W/m² difference from the reference in which neither is considered (Lohmann and Hoose, 2009). Storelvmo et al. (2008) also parameterized WBF in a model while simultaneously accounting for immersion and contact INPs. They yielded a warming effect that counteracts the cooling theorized to occur as a result of warm clouds (Storelvmo et al., 2008).

While these projects and others have been important in minimizing select uncertainties regarding mixed-phase clouds, the scientific community is still far from a comprehensive understanding. In the past fifteen years, research has refined several aspects of mixed-phase clouds: the scope of efficient INPs, yielding the prominence of mineral dusts and particularly feldspar-rich mineral dusts; the water-topped layered structure of mixed-phase clouds; the importance of WBF in activating and growing ice crystals; and the relationships among temperature, dynamics, and water-to-ice ratio.

Though there are components of mixed-phase clouds that are well understood, there is still significant uncertainty. The aforementioned experiments and others have provided helpful insight, yet a solution to the complex mixed-phase cloud problem can only be advanced by substantial experimentation, specifically in-situ measurements. These measurements require appropriate technology be developed to equip scientists with the best possible tools, the motivation for this work.

3. Methodology

Before introducing the new instrument that is the main focus of the work, it is important to briefly survey the current instruments and techniques that are being used in the field. There are many recent improvements in mixed-phase cloud sampling technology, which may help make more thorough observations of CCN, INPs, and mixed-phase cloud properties in the future. In this chapter, I will discuss some of the recent instruments being used to study mixed-phase clouds as well as introduce 3D printing technology.

3.1. Mixed-Phase Cloud Sampling Technology

There are many instruments currently in use to answer the two main questions surrounding mixed-phase cloud formation. First, what are the proportions of IWC, LWC, and TWC in the cloud? By narrowing down the phase partitioning of the clouds, researchers can better estimate other model parameters such as albedo, precipitation rates, and cloud lifetime (Abel et al., 2014; Korolev et al., 2003; McCoy et al., 2016). Second, what are the underlying aerosols that initiate cloud formation by acting as CCN or INPs? Understanding the chemical and physical properties of these aerosols can help modelers predict where clouds will form and how they will change in the future (Boucher et al., 2013).

3.1.1. Overview of Instruments

Currently, there is a variety of instruments that can estimate IWC, LWC, and TWC. Each instrument can be generally described as being made up of two components: an initial inlet that separates the different phases and a hygrometer or spectrometer capable of measuring the quantity of particles of each phase. Often, these instruments are coupled with a gas-phase hygrometer, which can measure the water vapor. Because TWC is the additive sum of IWC, LWC, and water vapor, knowing only three water content parameters yields all four. Three examples of probes that effectively measure two or more parameters are the Nevzorov Probe (Abel et al., 2014; Davis et al., 2007a; Korolev et al., 1998), the Isokinetic Total Water Content Evaporator (Strapp et al., 2016), and the Closed-Path Tunable Diode Laser Hygrometer (Davis et al., 2007b). These three instruments are summarized in Table 1.

The Nevzorov Airborne Hot-Wire LWC-TWC Probe, as described by Korolev et al. (1998), has been used in a number of aircraft observational studies of mixed-phase clouds. The probe is an example of a hot-wire instrument; it uses heat transfer calculations to determine the LWC and TWC (Abel et al., 2014; Davis et al., 2007b; Korolev et al., 1998). This is accomplished by holding the probe at a constant temperature capable of evaporating liquid water and measuring how much heat loss occurs in the wire following impaction by condensed water (Abel et al., 2014; Korolev et al., 1998). This probe is coupled with a TWC probe. The Nevzorov probe yields an accuracy within 10-15% (Korolev et al., 1998), yet it is only capable of directly measuring TWC and LWC. Regions of higher IWC can be inferred by comparing TWC and LWC.

The Isokinetic Total Water Content Evaporator (IKP-2), as described by Strapp et al. (2016), is also a hot-wire instrument and operates under a similar principle. The IKP-2 attempts to increase efficiency of ice crystal transmission by using an isokinetic inlet system in line with the hot-wire evaporation system (Strapp et al., 2016). An isokinetic inlet system achieves controlled, constant flow and a concentrated stream of aerosols by converging all of the flow

streamlines. In using an isokinetic inlet, the probe is capable of measuring TWC within 20% of the calibration values (Strapp et al., 2016).

The Closed-Path Tunable Diode Laser Hygrometer (CLH) described by Davis et al. (2007) uses evaporation and a sub-isokinetic inlet. A sub-isokinetic inlet is distinct from an isokinetic inlet because it results in both particle concentration and velocity enhancement by not becoming entrained in the flow streamlines in the inlet. Unlike the hot-wire techniques, the evaporation mechanism employed by the CLH to determine TWC measures differences in water vapor resulting from evaporation of condensed water (Davis et al., 2007a, 2007b). By using a sub-isokinetic inlet, the large particle concentrations are enhanced, yielding an enhanced TWC from which IWC can be calculated as long as ambient water vapor is measured simultaneously (Davis et al., 2007b).

These three instruments provide examples of tools used to address the relative proportions of ice crystals to water vapor, but they fail to collect the underlying CCN and INPs for analysis. An example of an instrument which seeks to reveal more about the ice crystals is the Cloud Particle Imager (CPI) described by Lawson et al. (2001) and Kuhn and Heymsfield (2016). The CPI is a high-resolution imager, capable of taking pictures of ice crystals in situ with a pixel size of 2.3 μm (Kuhn and Heymsfield, 2016; Lawson et al., 2001). From these images, information can be extracted such as crystal shape, refraction, and size, as well as estimates of IWC and particle size distribution. When mounted on a balloon, there is the advantage of being able to sample a strictly vertical profile of a cloud, as the balloon will move horizontally with the cloud it is inside (Kuhn and Heymsfield, 2016).

While the CPI is beneficial because it allows researchers to study single ice crystals, it still does not capture the underlying INP. In order to understand the properties of CCN and INPs, it is critical that the droplets and crystals are captured in a way that the residual can be preserved. One instrument capable of capturing droplets and ice crystals and re-directing them to instruments that can further study them is the Counterflow Virtual Impactor (CVI) and its laboratory counterpart the Pumped-Counterflow Virtual Impactor (PCVI).

3.1.2. Counterflow Virtual Impactors

One common method for studying CCN and INPs is derived from the idea that activated droplets or ice crystals are significantly larger than inactivated aerosol (Slowik et al., 2011); by separating based on size, researchers can study differences between CCN, INPs, and interstitial aerosol. This technique has been used in a large number of studies since the mid-1980s when Ogren et al. (1985) first described a technique of using aerodynamic properties to separate atmospheric trace gases from cloud droplets. The evolution of this technique is summarized in Table 2 along with further developments discussed in Section 3.1.3.

In its original stage of development, this technology was mostly used on airplanes to take in-situ measurements of clouds. The CVI is a device that harnesses the airflow created by aircraft movement to sample and size-select particles (Lin and Heintzenberg, 1995; Ogren et al., 1985). The key is the creation of a stagnation plane, a line in space where airflow streamline velocity is zero (Lin and Heintzenberg, 1995). Only particles with sufficient inertia – those that are aerodynamically large enough – can propel themselves past this area of no velocity to be entrained in a sample flow for further investigation.

CVIs have been coupled with a number of different instruments to learn different properties of CCN, INPs, and aerosols. For example, the Cloud Spectrometer and Imager (CSI) couples a CVI with a Lyman-alpha hygrometer to measure enhanced condensed water content as

a result of evaporation of the larger droplets and ice crystals (Davis et al., 2007a). A similar setup was used by Abel et al. (2014) in their comparison of the effectiveness of measuring IWC versus the Nevzorov probe, a total water probe, and an integration of ice crystal density. Coupling a CVI with a Lyman-alpha hygrometer, they found that the measured IWC agrees with the Nevzorov probe (Abel et al., 2014).

In 2006, a ground-based sampling method using vacuum-pumped air to generate the flow required to create a stagnation plane instead of an aircraft was described in detail (Boulter et al., 2006; Hiranuma et al., 2016a). Boulter et al. (2006) designed the PCVI apparatus to perform the same measurements without an airplane or wind tunnel. A vacuum pump is used to provide a “pump flow” (PF), while a compressor creates pressurized air to be introduced as an “add flow” (AF) to the PCVI. At the top of the PCVI is the “input flow” (IF) and at the bottom the “output flow” or “sample flow” (SF) is created (Boulter et al., 2006; Friedman et al., 2013). Together, the AF and PF create an “effective counterflow” (ECF) which counteracts the IF. A schematic of the PCVI flows is shown in Figure 1.

The AF and PF values regulate the cut-off size of aerosols that can pass through the PCVI. The 50% cut size or “D50” describes the lower bound of particle size that is transmitted through the PCVI at 50% transmission efficiency. For the PCVI to work, the AF must be larger than the SF to create the ECF (Boulter et al., 2006; Kulkarni et al., 2011). The ECF is necessary to create the stagnation plane. The other critical flow value that can be adjusted to change the particle cut size is the IF into the PCVI, which can be adjusted by changing the PF. In many cases, this IF is dependent on the other flows when doing sampling (Kulkarni et al., 2011; Slowik et al., 2011).

The PCVI can also act as a size-separating concentrator, which enhances particle counts. The PCVI removes the input gas and all particles smaller than the D50. Particles larger than the D50 will be entrained into the SF where the carrier gas is only made up of the AF. The enhancement should be roughly equal to the ratio of IF-to-SF (Slowik et al., 2011), though it is possible that it could exceed this theoretical enhancement factor. Performance studies and numerical model analyses were performed on both the CVI and PCVI. With both devices, the numerical models showed that the theoretical streamlines and performance aligned very well with the experimental results (Kulkarni et al., 2011; Lin and Heintzenberg, 1995).

Based on computational fluid dynamic (CFD) modelling, Kulkarni et al. (2011) suggest potential improvements on the PCVI. They suggest five aspects of improvement: redesign of nozzle free jet surface to minimize loss due to turbulence; redesign of nozzle geometry to reduce non-uniform counterflow velocity; adjustment of nozzle length and angle to maximize transmission efficiency; usage of a mixing volume to make output more homogeneous; and improved understanding of effects on complex, non-spherical shaped particles.

Since the original characterizations by Boulter et al. (2006) and Kulkarni et al. (2011), the PCVI has been used in many studies. As an example, Slowik et al. (2011) described a system for characterizing CCN using a PCVI. It is cited that it would not be possible to do this type of measurement without a PCVI (Slowik et al., 2011). The PCVI was also cited to be useful in other recent studies (examples: Baustian et al., 2012; Friedman et al., 2013).

3.1.3. Cloud Phase Separation Devices

Since CVIs are only capable of segregating particles based on different inertias, they must be coupled with some other system to differentiate between phases. There have been a few attempts building a system for characterizing the different phases of mixed-phase clouds that

incorporated CVIs. Of these, I will now discuss three. In each of these systems, the goal has been to sample only ice crystals from these clouds. The three examples chosen were selected because they involve either a CVI or PCVI in their attempt to separate ice crystals from water droplets and interstitial aerosols. The presence of a virtual impactor allows each of these inlets to sample the ice crystals in an adjoining instrument such as a spectrometer or particle counter. These three instruments are summarized in Table 2.

The Ice-CVI is a ground-based, vertically-aligned system that uses a series of virtual impactors to segregate particles based on size and water phase (Mertes et al., 2007). The Ice-CVI system aims to separate ice crystals from cloud droplets and interstitial aerosols based solely on size (Mertes et al., 2007). The basic design incorporates four stacked components: the omni-directional inlet, a virtual impactor, a pre-impactor, and a CVI. The omni-directional inlet and virtual impactor remove the largest particles, preventing any precipitation particles or other debris from entering the inlet. The omni-directional inlet has a theoretical limit of particles sizes below 50 μm in diameter while the virtual impactor will remove particulates larger than 20 μm in diameter (Mertes et al., 2007). Next, the pre-impactor uses impact freezing to remove super-cooled droplets. In this section, a cold plate is held in the pathway of the airflow. Ice crystals should bounce off of the impaction plates while the super-cooled droplets instantaneously freeze upon impact (Mertes et al., 2007). Finally, the particles are passed into a CVI, where the interstitial aerosols are removed from the ice crystals. The end result of this system is a steady flow of ice crystals between 5 and 20 μm in diameter (Mertes et al., 2007).

The Ice Selective Inlet (ISI), as described by Kupiszewski et al. (2015), segregates INPs from mixed-phase clouds using a series of aerodynamic separators and an evaporation unit. Similarly vertically-aligned, the ISI consists of the following components: an omni-directional inlet, a cyclone, a droplet evaporation unit, and a PCVI (Kupiszewski et al., 2015). First, an omni-directional inlet removes all of the large precipitation or other debris, as was done in the Ice-CVI. Next, the particles larger than 20 μm in diameter, mostly large ice crystals and droplets, are removed from the system by a cyclone. The droplet evaporation unit takes advantage of the WBF process; it is held at a constant low temperature, creating an environment with a super-saturation above saturation vapor pressure of ice but below that of water (Kupiszewski et al., 2015). Thus, the droplets evaporate while the ice crystals do not. Finally, the ice crystals, droplet residuals, and interstitial aerosols enter a PCVI, where only ice crystals are large enough to pass the stagnation plane to be entrained in the sample flow.

Another system that incorporates PCVI/CVI technology is the Ice-Selecting PCVI or “IS-PCVI” as described by Hiranuma et al. (2016). The PCVI in the IS-PCVI setup works like the PCVI described in Kulkarni et al. (2011) but at a larger scale (Hiranuma et al., 2016a). Due to its larger size, the IS-PCVI can achieve cut sizes as high as 30 μm , as opposed to the traditional PCVI which has an upper bound around 5 μm (Hiranuma et al., 2016a). In developing the IS-PCVI, four of the improvements suggested by Kulkarni et al. (2011) were incorporated; these include longer nozzle length, wider nozzle diameter, larger length-to-diameter ratio of the nozzle, and shallower inlet converging angle (Hiranuma et al., 2016a). Following validation experiments performed on the IS-PCVI, it is demonstrated that the IS-PCVI is capable of size-selecting for ice crystals larger than 10 μm without significant inadvertent transmission (Hiranuma et al., 2016a).

One significant limitation to these three inlets is the inability to simultaneously sample droplets and interstitial aerosol with the ice crystals. All three inlets separate out the ice crystals and pump away the droplets and interstitial together as a by-product. In order to fully understand

mixed-phase clouds, it may be necessary to have a more comprehensive picture of a single cloud. An ideal inlet would have three distinct channels through which interstitial aerosols, water droplets, and ice crystals can be simultaneously investigated.

There are other limitations on the availability and efficiency of the CVI and PCVI. For example, the cost is a barrier to entry for many groups who may want to use these instruments but cannot afford the costs. These costs exist in both time and money, as these devices are difficult and time-intensive to machine. Additionally, there are mechanical and structural limitations on these instruments. The PCVI, for example, has a very delicate inlet nozzle causing particle losses and a reduction in transmitted particles if misaligned. There are also limitations on classical machining when building a complex instrument like a PCVI.

3.2. 3D Printing Techniques

The 3D printing technology was first developed in the late 1970's and early 1980's and has since radically changed the prototyping process (Jacobs, 1992). Giving researchers, engineers, and students the ability to rapidly create models and parts, 3D printing could be greatly utilized to advance instrumentation in atmospheric science. This study is one of the first in cloud sampling devices to utilize this technology, thus it is appropriate to discuss the history and developments in relevant forms of 3D printing.

The most recent advancement in cloud phase separation devices is the ability to build a PCVI using three-dimensional (3D) printing (Koolik, 2016). 3D printing allows rapid prototyping for complex devices (Jacobs, 1992), making the development of more efficient and cheaper PCVIs possible. This development could potentially mitigate costs, decrease machining time, misalignment issues, as well as rapidly test various structural improvements such as those suggested by Kulkarni et al. (2011). In the study using a 3D printed PCVI, the print took only a few hours, whereas the time required to machine a PCVI can be weeks (Koolik, 2016).

3.2.1. Additive Manufacturing Overview

Additive manufacturing ("AM") is a term used to describe technology which creates objects from computer-generated 3D models by binding material together (Kudelski et al., 2017). The material being joined to form the part can be a number of different materials from metal powder to liquid plastic (Bhushan and Caspers, 2017; Kudelski et al., 2017; Wong and Hernandez, 2012). AM has the ability to generate parts quickly and with a high degree of accuracy.

AM has significant advantages over traditional machining for part generation and prototyping. First, AM reduces waste and resource consumption by eliminating the need for many materials and tools required for traditional machining (Kudelski et al., 2017). With AM, there is no longer a need for molds or dyes and there is little to no material waste generated from the additive process. Second, AM produces parts much faster than traditional machining (Bhushan and Caspers, 2017; Wong and Hernandez, 2012). This facilitates the generation of prototypes and the ability to catch errors in designs more quickly. Third, AM allows engineers to experiment with designs and geometries that were too difficult to manufacture using traditional machining (Kudelski et al., 2017). This is particularly relevant in this study, in which parts with complex internal features needed to be printed.

AM covers a variety of processes. These processes include, but are not limited to, Selective Laser Sintering (SLS), Fused Deposition Modeling (FDM), Laminated Object

Manufacturing (LOM), and Stereolithography Apparatus (SLA). These four techniques are summarized in Table 3.

SLS is the process of binding powdered material together via laser (Bhushan and Caspers, 2017; Kudelski et al., 2017; Wong and Hernandez, 2012). In this process, the 3D model is cut into cross-sections. Each layer is selectively hardened from the powdered material via a laser. As the laser finishes the shape of the cross section, the platform moves to make way for the next layer to be joined on top. Because the material is a solid powder, the resolution and accuracy of this technique is controlled by the material grain size. As a result, it generally has a lower resolution than other methods (Bhushan and Caspers, 2017; Wong and Hernandez, 2012). One advantage of SLS is that the powder itself supports the body of the object, so there is no need for additional support structures (Kudelski et al., 2017). However, single prints tend to be costly and time-intensive (Kudelski et al., 2017).

FDM builds an object layer by layer by depositing melted material (Bhushan and Caspers, 2017; Kudelski et al., 2017). As with SLS, the 3D model is divided into cross-sections and created in a layer-by-layer process. In FDM, however, a plastic material is drawn through a heated extruder nozzle where it melts. This material is then deposited onto the build platform, which moves down at the end of each layer. Unlike SLS, FDM requires the use of scaffolding to support the deposited material. FDM features low costs and minimal post-processing, but it struggles with low strength, warping, and poor resolution, which is directly related to nozzle size (Bhushan and Caspers, 2017; Wong and Hernandez, 2012). In comparing SLS and FDM, Kudelski et al. (2017) recommend the use of FDM for quick, simple parts and SLS for large-batch production.

LOM creates parts using sheets of material that are joined together and cut to proper size (Bhushan and Caspers, 2017). In this process, the cross-sections of the parts correspond to distinct sheets of material. At the start of a new layer, the sheet is joined to the sheet below. Then, a laser draws the cross-section to disconnect excess material, which can then be used as support structures. LOM is relatively inexpensive but the resolution is limited by the thickness of the sheet, which so far results in low resolution (Bhushan and Caspers, 2017).

There are many other processes for 3D printing, and many engineers are working to develop new ones. The last major technique for 3D printing is SLA. Because SLA is used for this project, it will now be discussed in more detail.

3.2.2. Stereolithography Apparatus (SLA) Printing

SLA refers to the process of creating an object by selectively hardening a liquid photopolymer resin using an ultraviolet laser (Bartolo, 2011; Bhushan and Caspers, 2017; Hagiwara, 2004; Jacobs, 1992; Wong and Hernandez, 2012). In SLA, the laser draws each cross-section of the object, causing photopolymerization of the resin. At the end of each layer, the build platform is moved up in a discrete step and the process is repeated.

The idea of using photopolymerization to create objects can be traced back to ancient civilizations, but the modern SLA approach dates back to the early 1970s (Bartolo, 2011). Between 1971 and 1985, a few models for creating 3D objects using photoreactive polymers were proposed (Bartolo, 2011), but the apparatus that most closely resembles the modern SLA printer was proposed by Charles Hull in 1986 (Hull, 1984). Hull (1986) proposed a system in which the build platform was facing downward into a bath of resin. The computer-controlled laser would draw the cross-sectional shape from below and then the build platform would move

upward at the conclusion of each layer (Hull, 1984). This device very closely resembles the modern, commercial SLA printer and the one used in preparing this project.

Bartolo (2011) summarizes the process of creating an SLA print into a series of steps. First, the user must create a model of their object using a computer-aided design (CAD) system. This model is then exported into a Standard Tessellation Language (STL) file format (Bartolo, 2011; Jacobs, 1992; Wong and Hernandez, 2012). STL files utilize triangles to represent the shape of the object and then split the object into slices (Wong and Hernandez, 2012). Third, scaffolding is added to support the part. Next, the printer receives the object's data and the model is built by selective laser photopolymerization. Once the printer is done, the object can be removed for post-processing. Post-processing involves removing the support structures, cleaning the object with a solvent to remove excess liquid resin, and post-curing in UV light.

There are some crucial advantages of using an SLA system that are important for the applications of environmental instrumentation. Primarily, SLA yields very high resolution and surface quality since these are both factors of laser precision (Bhushan and Caspers, 2017). This method also yields very little shrinkage or distortion relative to other processes of AM (Hagiwara, 2004). Yet, there are still drawbacks and common errors that occur with SLA. For example, overcuring, in which solidified material failed to bind with the layer below it, has been known to occur (Wong and Hernandez, 2012). Additionally, post-processing for an SLA part can be time-intensive (Jacobs, 1992; Wong and Hernandez, 2012).

Overall, SLA is a powerful form of AM in that it provides the ability to create parts quickly and with high accuracy. SLA has been used in multiple industries to create prototypes, models, prosthetics, art, and more (Wong and Hernandez, 2012). In this work, SLA is used to create many parts of a new instrument capable of discriminating between different cloud particulates.

4. Design and Development of Cloud Phase Separation Inlet

There is still a lack of knowledge and in-situ measurements on mixed-phase clouds. Therefore, we designed an instrument that can answer the two questions posed in Section 3.1.1.: What are the proportions of IWC, LWC, and TWC? What are the underlying aerosols that initiate cloud formation by acting as CCNs or INPs?

This study describes a new system harnessing the power of modern 3D printing techniques: the phaSe seParation Inlet for Droplets, icE residuals, and inteRstitial aerosols (SPIDER). It incorporates two 3D-printed PCVIs and a droplet evaporation chamber in order to provide simultaneous, comprehensive sampling of interstitial aerosol, droplet residuals, and ice crystal residuals.

In this chapter, I will describe the design and development processes used to create SPIDER. First, I will explain the theory of operation and discuss how SPIDER will segregate interstitial aerosols, droplet residuals, and ice crystal residuals. Thereafter, I will describe the physical manufacturing process and introduce the incorporated commercial instruments.

4.1. Theory of Operation

SPIDER is a vertically-aligned inlet system that has three distinct outlet channels for sampling interstitial aerosols, droplet residuals, and ice crystal residuals (Figure 1). It can be roughly broken down into the following four components: omni-directional inlet, L-PCVI, droplet evaporation chamber, and PCVI.

The omni-directional inlet prevents entry of large particulates, such as rain or debris, into the system. It was designed using Solidworks and printed on the Form2. A schematic of the omni-directional inlet is included in the Appendix. The opening slit of the inlet narrows from 4 mm down to 3 mm before the particles enter the inlet fully. Once inside the inlet, particles are forced to move upwards before entering the system. Particles too large to follow the streamlines will be lost due to impaction.

Directly downstream of the omni-directional inlet is the L-PCVI. The L-PCVI was designed in Solidworks based on the design of Hiranuma et al. (2016)'s IS-PCVI (Hiranuma et al., 2016a). A schematic of the L-PCVI design is included in the Appendix. As described by Hiranuma et al. (2016), when operated with a 70 LPM input flow and 7 LPM counterflow the L-PCVI is capable of achieving a D50 of approximately 9 μm . By operating the L-PCVI with an AF-to-IF flow ratio of 0.19, the D50 should be approximately 20 μm . At this D50, only activated droplets and ice crystals are large enough to enter the evaporation chamber as unactivated interstitial aerosol at high altitudes are typically no larger than 0.1 μm whereas cloud droplets and ice crystals are typically 10 μm or larger (Kleinman et al., 2012; Pruppacher and Klett, 1997; Rogers and Yau, 1989). The exact flow rates used in SPIDER are described in Table 4.

Calculations were performed using the flows of the L-PCVI to ensure that large droplets and ice crystals would be able to transmit through the L-PCVI without disrupting. To do this, the Weber Number was calculated using the conditions for typical SPIDER operation to find the maximum diameter of a droplet that can be transmitted under a various flow rates. The Weber Number, N_{We} , describes the ratio of the Bernoulli pressure caused by surrounding and opposing flow on a falling droplet to the surface tension of the droplet (Pruppacher and Klett, 1997). Droplet disruption has been estimated to occur for N_{We} significantly larger than 10 in laboratory studies (Pruppacher and Klett, 1997). For calculations done, the following expression was used to solve for N_{We} and maximum droplet diameter (d_{max}):

$$(1) \quad N_{We} = \frac{\rho_a d_{\max} U_{\infty}^2}{\sigma} = \frac{8}{C_D}$$

$$(2) \quad d_{\max} = \frac{8\sigma}{C_D \rho_a U_{\infty}^2}$$

where ρ_a refers to density of the surrounding air, σ is the surface tension of the droplet, U_{∞} is the difference between the droplet velocity and the gas velocity, and C_D refers to the drag coefficient (Pekour and Cziczo, 2011). The droplet velocity was approximated using the following expression from Pekour and Cziczo (2011):

$$(3) \quad \frac{m_p v_i^2}{2} = \frac{m_p v_{i-1}^2}{2} + \Delta x \cdot F_{D_{i-1}}$$

$$(4) \quad F_D = \frac{\pi C_D \rho_a v^2 \chi^2 d_{\max}^2}{8 C_c}$$

where C_D refers to the drag coefficient, χ is the shape factor, and C_c is the slip factor.

A MATLAB-script was written to calculate the Weber number as a function of distance along the L-PCVI. The results of this calculation are shown in Figure 3. Using SPIDER's L-PCVI IF of 42 SLPM, the Weber number was calculated for droplets varying in size from 1 μm to 75 μm . The largest droplet had the largest Weber number, but its maximum Weber number was approximately 0.3, signifying that it will not break up in the L-PCVI using SPIDER's flow rates since this is much lower than 10.

Once the ice crystals and supercooled droplets pass through the L-PCVI, they enter the droplet evaporation chamber. The droplet evaporation chamber operates under the principle of the WBF process. By holding the chamber at a constant temperature above the supersaturation with respect to ice and below the supersaturation with respect to water, the droplets will evaporate while the ice crystals stay a constant size or grow slightly at the expense of the evaporating droplets. The ideal temperature to achieve this supersaturation is -16°C , where the difference in saturation vapor pressure between water and ice is at maximum. Thus, by the end of the chamber, the ice crystals and water droplets will exist in two separate size modes.

Attached directly below the droplet evaporation chamber is the PCVI. The PCVI can be either industrially manufactured (Model 8100, BMI Inc.) or 3D printed. The PCVI in SPIDER is similar in dimensions to the one described in Boulter et al. (2006), Kulkarni et al. (2011), and Koolik (2016). As described in Section 3.1.2., the fundamental flows through the PCVI are the AF, PF, SF, ECF, and IF. In the SPIDER setup, the PCVI is operated with the following flows, achieving a D50 $\sim 2 \mu\text{m}$ (Koolik, 2016; Kulkarni et al., 2011): AF = 2.0 SLPM, PF = 7.68 SLPM, and SF = 0.74 SLPM, resulting in an IF = 6.78 SLPM. With the D50 of $\sim 2 \mu\text{m}$, it is expected that the ice crystals will pass through the stagnation plane to be entrained into the SF of the PCVI while the droplet residuals will be rejected and exit through the PF. These flows are summarized in Table 4.

The Weber number was also calculated for the PCVI (Figure 4). The Weber number in the PCVI was higher for all of the droplets than it was in the L-PCVI. This is because the gas velocity is higher due to the smaller area. Even though the flow rate is lower than in the L-PCVI, the velocity still increases due to the difference in area. Still, the maximum Weber number for the largest droplet is below the threshold of 10, signifying that droplets will not break up within the PCVI either.

The final product of SPIDER is therefore an opportunity for simultaneous sampling of interstitial aerosol, droplet residuals, and ice crystal residuals. The three outlet channels – the PF of the L-PCVI, PF of the PCVI, and the SF of the PCVI, respectively – can be connected to chemical composition analyzers or optical particle counters for further analysis.

4.2. Design and Construction

Between February and April 2017, SPIDER was built from scratch to a fully functional instrument. This was only possible due to the combination of different tools. Solidworks was used to generate a CAD of the whole system as well as to design new and unique parts. The Form2 printer was used to rapidly create the designed parts to be integrated into SPIDER, while the housing and panels of SPIDER were classically machined. I will now discuss the design and construction processes for SPIDER in more detail.

4.2.1. Computer Aided Design Using Solidworks

Solidworks is a CAD software that allows the user to draw intricate 3D parts and run analysis on them. For this project, Solidworks was mainly used to create parts to be custom-fitted and 3D printed for SPIDER. Although there is a potential for future use of fluid modeling add-ins in the software, limited simulations were performed in this study.

While designing SPIDER, there were many parts that were designed to perfectly fit the mechanical needs of the structure. In these cases, the following procedure occurred. First, measurements were taken of the exact dimensions required for the part. Next, a part was sketched by hand to design the overall shape or concept of the part. After being sketched by hand, the part was drawn in Solidworks. On occasion, the Solidworks assembly tool was used to verify that certain parts would fit together as designed.

Using this procedure, the parts were tested in Solidworks before being printed. These parts include but are not limited to: support brackets, fasteners, hinges, Arduino casings, temperature sensor holders, droplet evaporation chamber holders, the PCVI, the L-PCVI, as well as the omni-directional inlet.

4.2.2. 3D Printing Using Formlabs Form2

From Solidworks, the part file was exported as a stereolithography file (.STL) and uploaded to the 3D printing software (Preform, Formlabs Inc.). Preform reads the .STL format and allows the user to orient and add support structures to the part. Support structures have very small contact points (0.5 mm) attached to the part for easy removal during post-processing. Before uploading, Preform runs a calculation to determine whether a print will be successful or not.

From Preform, the part is uploaded onto the printer (Form 2, Formlabs Inc.). The Form2 uses a 405 nm UV laser to cure the specific locations, based on the designed part, in the resin bath for each layer (Formlabs, 2015). For each vertical layer of the drawing, the laser beam cures a cross-section of the design from liquid to solid. The Form2 can print layers at 25, 50, or 100- μ m resolution. For the parts incorporated into SPIDER, tough resin (FLTOTL03, Formlabs Inc.) printed with 100- μ m resolution was used.

After a print was completed, the parts were post-processed following the procedure described by Roesch et al. (2017). First, the parts are removed from the build platform and placed in a bath of isopropyl alcohol (IPA). The parts are shaken in the bath and then left for approximately 20 minutes to remove uncured resin (Roesch et al., 2017). Next, the parts are exposed to UV light inside a curing box with a similar wavelength to the printer's laser. The time spent in the UV-chamber depends on the size and complexity of the object, though many of the parts incorporated in SPIDER were placed in the curing box overnight. This further hardens and strengthens the plastic. After, the support structure was removed, bumps or stumps left by the

support were wet-sanded using P240 and P1200 grit in succession to smooth the surface of the part.

4.2.3. Mechanical Construction

It is estimated that SPIDER is built of ~60% 3D printed parts by number, but many parts needed to be machined or bought commercially in order to complete the construction of the inlet system. A Solidworks drawing of SPIDER is included as Figure 2, for reference. This schematic is to scale, and shows the physical structure, as well as the L-PCVI, the droplet evaporation chamber, and the PCVI. This schematic neither includes any of the acrylic panels nor the insulation surrounding the evaporation chamber.

SPIDER is designed to have two modular components: the chamber housing and the electronics housing. Each module is housed by 1-inch black anodized aluminum T-slotted framing. The outside of SPIDER is paneled with acrylic glass. The aluminum T-slotted framing is connected using 3D printed 1-inch cubes.

The top module houses the droplet evaporation chamber. This module is a rectangular prism that stands 53 inches tall with 11 inch square bases. It has two support shelves, each approximately 10 inches off the individual bases and one in the middle of the rectangular prism. Attached to these shelves are the chamber holders, supporting the chamber in three locations. Each shelf is supported by 3D-printed 2-inch braces, which connect them to the main framing.

The bottom module is a 19 inch cube. It has two pieces of T-slotted aluminum across the top that allows the top module to be mounted directly onto it. The top module is connected via a 3D-printed U-clamp. The U-clamp is fitted to the size of the T-slotted framing and has holes that allow it to be fastened using screws. Approximately halfway down the cube, there is an acrylic glass shelf with a square cut out of the center. This shelf holds the mass flow controllers (MFC, MCS Series, Alicat Inc.). The center cut-out allows the PCVI to sit within the cube. The bottom module is mounted on heavy-duty casters for easy transport.

Additionally, the top module with the chamber is supported by four “legs”. These legs connect from the upper part of the top module to the outside perimeter of the bottom module. They are connected via 3D-printed pivots, which also allow for vertical alignment of the top module.

4.3. Incorporated Commercial Instrumentation

A number of commercial instruments were built into SPIDER. For the tests described in this work, optical particle sizing and counting instruments were used at the three particle collection channels. These provide information about the number and concentration of particles as a function of their particle diameter. If measurements were desired that instead provide information on chemical composition the counting instruments could be easily replaced.

4.3.1. Optical Particle Sizer

Data on particle size and number concentration from the sample flow of the PCVI were collected using the Optical Particle Sizer (OPS, Model 3330, TSI). The OPS uses light scattering to measure the size and number of particles as they move through the system. An internal laser beam is used to illuminate the particles. After scattering occurs, the OPS classifies particles into sixteen distinct bins based on particle diameter derived from the amount of light scattered. These bins range from 0.3 to 10 μm . The results are then communicated through the Aerosol Instrument Manager software (AIM, TSI Inc.) and analyzed using MATLAB.

Particles move through the system at a constant flow rate of 1.0 LPM(TSI, 2011). For this project, the OPS was reconfigured to run with an external pump. This was done to reduce pressure differentials and to assure that the 1.0 LPM flow rate was maintained.

4.3.2. Optical Particle Counter

Two Optical Particle Counter (OPC, OPC-N2, Alphasense) were installed, one in the PF of the L-PCVI and one in the PF of the PCVI. The OPCs operate similar to the OPS in that they use a laser source and measure the amount of light scattered to determine particle size and number. In contrast to the OPS, the OPCs detect particles in the range from 0.38 to 17 μm and the SF rate is approximately 0.22 LPM. Similarly to the OPS in SPIDER, the OPCs were reconfigured and driven by an external, controlled flow. While the OPS's flow was controlled by MFCs, the flows into the OPC were controlled by needle valves and verified by a gas flow calibrator (Bios, DryCal Definer 220, Mesa Laboratories).

4.3.3. Mass Flow Controllers

Flows were controlled by MFCs and verified by the Bios. The MFC are accurate within $\pm 0.8\%$ of their reported flow rates (Alicat Scientific, 2016). MFCs were connected to the PF and AF of both the L-PCVI and PCVI. Additionally, two MFCs were used to control the flow of the OPS. The MFCs were controlled remotely using a serial command.

4.3.4. Low Temperature Cooling Bath

In order to achieve the temperature required for WBF to evaporate droplets and maintain the ice crystals inside the chamber, it was necessary to use a low-temperature cooling bath (Proline RP 1290, Lauda-Koenigshofen). The unit works by pumping the cooling fluid from the base of the tank, which is held at a constant set temperature, into the system. The fluid is constantly flushed through the system to avoid solidification of the cooling fluid. For SPIDER, ethanol was used as cooling fluid. Ethanol allows the cooling bath to go as cold as -65°C .

4.3.5. Temperature Sensors

The temperature profile of SPIDER is monitored in sixteen different locations by 1-Wire digital thermometers (DS18B20, Dallas Semiconductor). The temperature sensors are functional from -55°C to $+125^{\circ}\text{C}$ with a $\pm 0.5^{\circ}\text{C}$ accuracy between -10°C and $+85^{\circ}\text{C}$ (Dallas Semiconductor, n.d.). The temperature sensors are located approximately every 100 mm from directly below the L-PCVI to directly above the PCVI. The temperature sensors are connected to Arduino, which allows data to be recorded to text file on a one second-resolution. These sensors have been noted in Figure 2 as "TS" including the number of the sensor.

5. Verification Experiments

Once built, it was critical to verify the theory by performing a series of laboratory verification tests. First, each major component of SPIDER was tested. Then, the system was assembled to ensure that all components work together.

5.1. Large Pumped Counterflow Virtual Impactor (L-PCVI) Cut-off Measurements

The L-PCVI was designed using the specifications from Hiranuma et al. (2016). Hiranuma et al. (2016) provides insight into the expected working conditions of the L-PCVI at different flow ratios. The operating ratio of AF to IF of the L-PCVI in SPIDER is approximately 0.19, using the AF and IF in LPM in laboratory conditions. Thus, the expected D50 of the L-PCVI is between 20-30 μm . The available instruments, the OPC and the OPS, can only detect particles up to 16 and 10 μm , respectively, so the two objectives of these measurements were to narrow the range of expected D50 and to prove that the L-PCVI rejects particles smaller than the D50 as described by Hiranuma et al. (2016) when matching their flows.

Two experiments were performed, each to achieve one of the goals. The first experiment served to find a lower bound of the D50 and prove that the L-PCVI rejects small particles at the flow rates used in SPIDER. By injecting particles of a known diameter smaller than the expected D50 and seeing them in the PF region, the D50 is proven to be larger than this particle diameter. The second experiment replicated measurements done by Hiranuma et al. (2016); droplets of a known size with an expected residual size were introduced into the L-PCVI. The residuals were then analyzed in the SF region.

5.1.1. Lower Bound of L-PCVI Experiment

To find the lower bound, 10 μm polystyrene latex (PSL) spheres were generated using a 1.7 SLPM flow into the PROTeGE wet particle generation system (Roesch et al., in preparation). Particles were first introduced into the L-PCVI having the PF and AF off. This provided information about the aerosol size distribution generated by PROTeGE. After sufficient number of samples to obtain an average size distribution, the flows on the L-PCVI were turned on. SPIDER was run with the flows described in Table 4 the PF was 42.5 SLPM and the AF was 10 SLPM. The experimental setup is drawn in Figure 5A.

One OPC was connected to the PF of the L-PCVI; another OPC and the OPS were connected to the SF of the L-PCVI. In the configuration with the L-PCVI off, it is expected that there would be no particles in the PF but many particles in the SF. When the L-PCVI flows are on, the opposite is expected. Samples were taken at a 1-second resolution for at least 100 seconds. This setup is drawn in Figure 5B.

The results of the 10 μm PSL measurements are summarized in Figure 6. Figure 6A and 6B show the average number concentration obtained in the PF and SF, respectively. The L-PCVI flows are initially off. While they are off, particles are only measured in the SF and not in the PF. The AF is turned on approximately 1900 seconds into the measurement. The PF is turned on approximately 100 seconds later. The results are inversely correlated, as expected. When the L-PCVI flows are off, the SF has a large concentration of 10 μm particles; when the L-PCVI flows are on, these particles appear in the PF and nothing appears in the SF. When only the AF is on, it is possible that the particles are being rejected through the IF, resulting in no detectable signals in the PF or SF. From this, it is concluded that the cut size of the L-PCVI must be larger than 10

μm , since there is no transmission of particles below $10\ \mu\text{m}$, even when a large number of solid $10\ \mu\text{m}$ particles are introduced into the IF.

5.1.2. L-PCVI Verification Test

In order to prove that the L-PCVI has the D50 projected on the best-fit line from Hiranuma et al. (2016), it is important to prove that the 3D-printed L-PCVI achieves similar results to the values that they obtained. The measurements by Hiranuma et al. (2016) used a SF of 2 LPM, but SPIDER requires that the SF of the L-PCVI be approximately 6.7 SLPM to provide the correct residence time in the chamber and the correct IF for the PCVI. Hiranuma et al. (2016) state in the supplementary material that varying the SF will not affect the D50 or performance of the L-PCVI. If the ECF is held constant, changing the SF will only influence the concentration. Using the 2 LPM SF from Hiranuma et al. (2016), the concentration of droplets is high enough to get a detectable residual concentration with the resulting IF.

The flow regime chosen from the literature for this experiment was an IF of 50 LPM and an AF of 7 LPM. Under these flows, Hiranuma et al. (2016) report a D50 of $21.99\ \mu\text{m}$. This has an AF-to-IF ratio of 0.14 whereas the SPIDER L-PCVI configuration has an AF-to-IF ratio of 0.19 using the flows in LPM that correspond to the SLPM flow values in Table 4 at the temperature and pressure of the laboratory. It is expected that a ratio of 0.14 will yield a smaller D50 than the D50 created by SPIDER's typical operation flows.

To create particles larger than this expected D50, droplets were generated using a commercial droplet generator ("DG", MD-K-130, Microdrop Technologies) with a $30\ \mu\text{m}$ nozzle. Using a high resolution magnification camera and image analysis software, the droplet size directly leaving the nozzle was approximately $50\ \mu\text{m}$ in diameter. However, a calculation of evaporation using the relatively dry air and distance to the inlet of the L-PCVI suggests that the droplets entering the L-PCVI are approximately $40\ \mu\text{m}$. Droplets were created from an ammonium sulfate (AS) solution of 5 g/L. The residuals size of these droplets were calculated to be approximately $3.7\ \mu\text{m}$.

First, a measurement of droplet transmission and residual size was performed. The schematic for this setup is drawn in Figure 7A. The DG was placed approximately 5 mm above the L-PCVI. Having this gap, it was possible to see the droplets enter the L-PCVI without any breakup. A stream of droplets was introduced through the L-PCVI without PF or AF on (Figure 8A). The OPS was connected to the L-PCVI with a flow splitter allowing the 2 LPM through the L-PCVI having 1 LPM as IF to the OPS and 1 LPM as bypass flow through a MFC. The results of this measurement indicate that the residual size after residence time in the apparatus is approximately $4.7\ \mu\text{m}$. This is slightly higher than the calculated residual size. This could potentially be due to the particles not being fully effloresced or evaporated by the time they reach the OPS.

Next, the L-PCVI flows were turned on and measurements of the resulting particles in the SF were recorded (Figure 8B). This schematic is shown in Figure 7B. Again, there is a peak of particles in the $4.7\ \mu\text{m}$ size bin, suggesting that the droplets are transmitting and then evaporating, leaving the residuals. The smaller particles that are transmitted may be due to inadvertent transmission through wake capture.

For completeness, the PF of the L-PCVI was shut down and only the AF was left on. The results of this test are shown in Figure 8C. Here, almost no particles are able to transmit through the L-PCVI. This proves that the particles collected in Figure 8B are the result of droplets large enough to pass through the stagnation plane.

5.1.3. Summary of L-PCVI Results

These two experiments provide sufficient information to approximate the D50 of the L-PCVI and prove that it works as expected. By proving that the D50 is within the range predicted by Hiranuma et al. (2016) using their flow ratio and values, it is shown that the 3D printed L-PCVI works. While it is not possible at the moment to further refine the D50 for the 3D printed L-PCVI due to a lack of an instrument with a detection range greater than 20 μm , it can be estimated that the L-PCVI is consistent with the findings of Hiranuma et al. (2016). Figure 9 shows the expected result superimposed onto a figure from Hiranuma et al. (2016). Further experimentation on the 3D printed L-PCVI should be done to resolve the D50.

5.2. Evaporation Chamber Temperature Calibration and Response Measurements

A test of the temperature of the chamber was performed to determine a set of working principles for running the chilling bath and the chamber at the temperature required for WBF to discriminate between droplets and ice crystals. The theoretical temperature necessary is -16°C . The purpose of this test was to determine how to achieve a chamber temperature of -16°C and how to sustain it.

5.2.1. Temperature Sensor Calibration

In order to ensure that the temperature sensors were providing an accurate readout of the actual temperature, a calibration was necessary. To perform this calibration, a holding tray was cut to take the place of the lid to the chilling bath. The holding tray was constructed from acrylic and had a four-by-four matrix of holes exactly the same size as the temperature sensors. During the tests, the tray was fixed to the top of the chilling bath such that the sensors could rest in the holes and be submerged in the cooling fluid.

The calibration curve was measured by running the chilling bath at a constant temperature for fifteen minutes and then stepping down by five degrees. Since SPIDER will primarily operate at -16°C , it was more important that the calibration curve be centered on low temperatures. For this reason, the calibration measurements started at a set temperature (T_{set}) of 0°C and ended at -40°C . Once the data was recorded, the average temperature was calculated from the measurements for each sensor at each T_{set} .

The average temperature of each sensor as a function of T_{set} is plotted in Figure 10. Also plotted in Figure 10 is a dashed line that represents perfectly matching T_{set} to the measured temperature. For all values of T_{set} and for all sensors, the measured temperature was warmer than T_{set} , yet the sensors clustered very closely together.

The resulting achieved temperature versus T_{set} data was put through a Python script to determine the best fit parameters for creating a linear function between measured temperature and actual temperature. In other words, for

$$(5) \quad T_{set} = \alpha T_{measured} + \beta$$

the values of α and β were derived using a fitting algorithm that took into account each $T_{measured}$ and T_{set} for each sensor. The result of the fitting script was a 2-by-16 matrix with α and β for each sensor. These constants were then incorporated into the Arduino code to record and report the calibrated temperature in future experiments.

5.2.2. Chamber Response Calibration

In addition to ensuring that the temperature read-out is the actual temperature, it is important to understand the response between the chilling bath and the measured temperature. This test facilitated an increased understanding about heat losses in the system.

For this experiment, SPIDER was set up in quasi-working condition. The temperature sensors were connected to the chamber, insulation was fully covering the outside of the evaporation chamber, and the chilling bath was connected to the inlet and outlet of the fluid ports on the flow chamber. The L-PCVI and PCVI were removed since they were not required for this test. Connected to the bottom of the chamber was a needle valve, which controlled the flow rate to approximately 6.7 SLPM measured by the Bios. This is the typical operating IF for the PCVI, so it is the flow rate that will be typical for the evaporation chamber when SPIDER is operating.

The mechanics of this calibration experiment were very similar to the sensor calibration tests. The T_{set} of the chilling bath began at 10°C and stepped by 5°C until the lowest temperature achievable in the bath, -60°C. At each temperature, data were recorded for fifteen minutes with greater than one sample per second resolution.

The same analysis was performed on the data collected in this experiment as the sensor calibration. For each sensor and at each T_{set} , an average measured temperature was obtained. The aggregated results of this test are shown in Figure 11. It is important to note that not all temperature sensors are within the ethanol-cooling region of the evaporation chamber: temperature sensors four through thirteen are touching the glass of the chamber where cooled ethanol is pumped through; sensors thirteen, fourteen, and fifteen are directly below the ethanol outlet, but still touching the glass; sensors one and sixteen are open to room air; and sensors two and three are touching the glass above the ethanol inlet. In this case, it should not be alarming that sensors one, two, three, and sixteen are not dependent on T_{set} .

There are two main interesting takeaways from Figure 11. First, sensor four is significantly cooler than the other chamber sensors at all values of T_{set} . Potential explanations for this behavior include heat losses at the inlet, failure of the sensors to fully touch the chamber, or failure of sensor four. Second, the measured chamber temperature is significantly warmer than the set temperature in the chilling bath. Figure 12 shows the data from only those sensors that touch the flow chamber. The shaded area represents the range of temperatures recorded by sensors five through thirteen. Because it is significantly colder than the other sensors, sensor four is plotted alone. This figure shows that it is not until temperatures cooler than -50°C that the chamber reaches the goal temperature of -16°C. This could potentially be reduced with better insulation and shorter tubing from the cooling bath to SPIDER.

This experiment demonstrated that the chilling bath should be operated between -50° to -60°C in to achieve the optimal response in SPIDER. However, temperatures below -40°C could lead to homogeneous freezing of droplets upon entry in the chamber. Homogeneous freezing would bias the system into counting more ice crystals than were originally present in the cloud. To prevent this from happening, the insulation of the system should be upgraded to prevent heat diffusion from the surroundings into the chamber. This will lower the set temperature required to achieve a stable chamber temperature of -16°C.

5.3. Flow Chamber Verification

Next, it is critical to verify is SPIDER's ability to evaporate droplets and to sustain ice at low temperatures. Without being able to do this, SPIDER cannot successfully segregate ice and water, even with a functioning PCVI.

5.3.1. Droplet Evaporation Modeling

In order to verify that droplets are able to evaporate in the chamber, a model of droplet evaporation was written based on the equation of evaporation described by Lohmann et al (2016)

$$(6) \quad r(t) = \sqrt{r_0^2 + 2 \left(\frac{S-1}{F_k + F_d} \right) t}$$

where r_0 is the initial droplet radius and S is the supersaturation. F_k and F_d are defined as

$$(7) \quad F_k = \rho_w \left(\frac{L_v^2}{K R_v T^2} \right)$$

$$(8) \quad F_d = \rho_w \left(\frac{R_v T}{D_v e_{s,w}(T)} \right)$$

where ρ_w is the density of liquid water, L_v is the latent heat of vaporization, D_v is the diffusion coefficient for water vapor in air, $e_{s,w}$ is the saturation vapor pressure of water, and K is the coefficient of thermal conductivity in air. This equation is valid for large droplets, as it neglects the effects of solution and curvature of the droplet. When sampling from clouds, the droplets should be sufficiently large for this assumption.

The model was run with the approximate chamber dimensions. The inner diameter of the chamber is approximately 5.15 cm. With a steady, controlled flow of 6.78 SLPM, the droplets move at a velocity of 5.42 cm/s. The length of the chamber is approximately 138.4 cm, providing a residence time in the chamber of about 25 seconds.

Figure 13 shows the results of the model for a variety of initial droplet sizes at different supersaturations. Droplets vary in initial size between 5 μm and 50 μm in radius. These droplets were modeled in supersaturations of 0.25, 0.5, 0.74, and 1. In the simulation where $S = 1$, all of the droplets retain their original size. In the other three simulations, the 5 and 12.5 μm fully evaporate by the end of the chamber. The 25 μm droplet evaporates fully when supersaturation is equal to or lower than 0.5.

From these models, a few statements can be made about the evaporation in the chamber. First, it is expected that droplets equal to or smaller than 12.5 μm in diameter will fully evaporate before reaching the PCVI. When running the simulation on these droplets under high levels of supersaturation, they evaporate fully up to supersaturations of approximately 0.9. Second, droplets between 12.5 and 25 μm in diameter will likely evaporate if the chamber supersaturation is below 0.5. Given that the 12.5 μm droplets evaporate halfway through the chamber when supersaturation was 0.75, it is likely that the smaller droplets in the range of 25-50 μm evaporate at supersaturations between 0.5-0.75 as well. Finally, droplets larger than 25 μm will likely not evaporate fully within the chamber at any supersaturation.

It is worth speculating on the range of the real supersaturation achieved within the chamber to have a better estimate of the range of droplets that will evaporate before reaching the PCVI. The chamber receives all of its flow from the L-PCVI. The L-PCVI has two conditions separated by the stagnation plane: ambient and dry. Above the stagnation plane, the air has the relative humidity (RH) of the environment it is sampling from. When sampling from a cloud, this condition will likely be supersaturated. However, below the stagnation plane the RH is set by the AF air, which is fully dried before entering the L-PCVI. Thus, the air going from L-PCVI to chamber is very dry. However, evaporation is continually occurring in the chamber, moving some water from the droplets into the vapor phase. This probably causes an increase in the RH inside the chamber. As a result, it is not unrealistic that the supersaturation in the chamber is closest to 0.25, evaporating even droplets larger than 25 μm .

Similarly, it is worth noting that significant evaporation will likely occur in the L-PCVI before the droplets reach the chamber. Droplets that are large enough to pass the stagnation plane

are blasted with dry air from the AF for the duration of their time in the L-PCVI. It is not, then, unrealistic to predict that even the largest cloud droplet will evaporate fully within the chamber once it undergoes evaporation in the L-PCVI.

Finally, when operating with the omni-directional inlet in line, it is unlikely that any droplets larger than 50 μm in radius will be able to pass through the omni-directional inlet. Some evaporation will also occur within the omni-directional inlet. Once these especially large droplets enter the L-PCVI, they should be evaporated even more in the L-PCVI. Overall, this suggests that it is unlikely that droplets significantly larger than 25 μm in diameter will enter the chamber.

5.3.2. Maintaining Ice Crystals

The second role of the chamber is to sustain ice crystals via the WBF process. In order for SPIDER to separate ice crystals from droplets inside the PCVI, ice crystals need to maintain the same size while droplet evaporation occurs.

To verify that ice crystals are maintained throughout the chamber, an experiment was done using the DG. Droplets of approximately 40 μm in diameter generated from a 0.6 g/L AS solution were introduced into the chamber close to the entry point of fluid from the chiller. The chamber was set to -65°C in order to homogeneously freeze the droplets. With this concentration of AS, literature suggests that homogeneous freezing should occur at approximately -36°C (Larson and Swanson, 2006). With the chiller set at -65°C , the temperature sensor closest to the fluid entry point recorded an average temperature of -40°C . The chamber was flushed with dry, filtered air for approximately two hours before measurements were taken.

The ice crystals then traveled down the chamber until the PCVI. The PCVI was run with the typical flows that achieve a D50 of approximately 2.7-3.8 μm . This range will be explained in Section 5.4.2. The results of the PCVI SF measurements are shown in Figure 14. Here, Figure 14A shows the results when the chamber was sampling only ambient room air. In Figure 14B, the DG was turned on. The difference of these two measurements is shown in Figure 14C to represent the contribution of the DG alone. The PCVI is on for both of these measurements.

There is a signature peak in the contribution from the DG reveals that the ice crystals are being maintained in size throughout the chamber. Given that the droplets are almost definitely freezing upon entry to the chamber, presence of residuals reveals that the ice is passing through the stagnation plane of the PCVI. A calculation of the residual size of AS expected yields approximately 1.4 μm . Given the shape of Figure 14C, it appears that the ice crystals are passing through the stagnation plane of the PCVI but not evaporating fully by the time they reach the OPS.

5.4. Pumped Counterflow Virtual Impactor (PCVI) Cut-off Measurements

Two experiments were performed to test that the PCVI was operating as intended. The tests emulate those of Boulter et al. (2006), Kulkarni et al. (2011), and Koolik (2016) in setup. The calibration experiments were designed to prove that the PCVI is capable of separating large ice crystals from evaporated droplet residuals.

5.4.1. Experimental Setup

The first of the two experiments was designed to compare the output from the pump flow with that of the sample flow. For this test, the L-PCVI and omni-directional inlet were removed from SPIDER. The PCVI was connected directly under the chamber. The top of the chamber was open to ambient room air, which was approximately constant throughout the measurements.

In the first step of this test, the OPS was connected to the SF of the PCVI. Measurements at 1-second resolution were taken for five minutes while the PCVI flows were off. In this configuration, the PCVI acts as a tube; it is expected that the measurements taken by the OPS will resemble ambient air size distribution. Next, the PCVI flows were turned on and the five-minute measurement was repeated. Finally, the OPS was disconnected from the SF and reconnected at the PF. If functioning correctly, this result should approximate an ambient distribution, with lower concentrations at higher diameters. Schematics of this setup are shown in Figure 15.

The flows used for this test were the same as those proposed for optimal PCVI performance (Table 4s). The PF was set to 7.68 SLPM and the AF was 2.0 SLPM; IF for the OPS was measured to be 0.74 SLPM using the Bios. All flows for these tests were controlled by MFC.

The second experiment involved using PSLs because they are a defined size and retain their size and shape very well. For this experiment, 5.0 μm PSLs were used. This diameter was chosen because it is sufficiently higher than the expected D50 that they should be transmitted through the PCVI. The goal of this experiment was to collect PSL particles out of the SF of the PCVI without significant inadvertent transmission of smaller particles. The setup of this experiment was the same as that of Figure 15, except that a controlled flow of PSLs was introduced into the IF of the PCVI.

PSL particles were generated out of solution using a medical nebulizer. The nebulizer was supplied a constant flow of 3 SLPM controlled by MFC. The solution was created by placing roughly 15 drops of PSL solution in approximately 100 mL of double-deionized water. While the concentration is not precisely known, it is expected that it will produce a relatively constant stream of particles while the volume of solution is sufficient. The atomizer works by mimicking the bubble burst process by which sea salt becomes aerosolized. Pressurized air at a constant and controlled flow rate is pushed through the center of the nebulizer, which causes the solution to bubble. When the bubbles burst, the aerosol is released into the air flow that enters the experimental system.

5.4.2. Results and Discussion

The results of the ambient air experiments are shown in Figure 16. Figure 16A shows the raw concentration of particles detected by the OPS when the PCVI flows were off and the OPS was connected to the PCVI's SF. Figure 16B is the result when the PCVI flows were turned on and the OPS was connected to the SF. Figure 16C shows the mean concentration of particles in each size bin when the OPS was connected to the PF and the PCVI flows were on.

A comparison of Figures 16A and 16C is necessary to determine that the PCVI is working correctly. In a functional PCVI, the small particles should be pumped away in the PF, so there should be a comparable number of particles in the small bins of the SF when the PCVI flows are on and in the PF when the PCVI flows are off. This is seen in Figure 16. The concentrations of particles in the three smallest bins from the operational PCVI's PF are within 15% of those recorded when the PCVI flows were off and the OPS was attached in the SF region. As the particle diameter approaches the expected D50, the concentrations are within about 50% of each other. It is expected that the concentrations of particles in the PF larger than the theoretical D50 will be significantly smaller than their counterparts in the SF sample because these larger particles are transmitting through the SF of the PCVI with flows on and not being

pumped away in the PF. This is seen in the data as the concentrations of particles larger than the D50 in the off PCVI's SF range from approximately 300-2800% of those in the PCVI's PF.

Additionally, a D50 was calculated for the PCVI of 3.8 μm from the measurements of ambient air rejection. To calculate the D50, the data was processed through a MATLAB script. An example of the resulting curve and sigmoidal fit is shown in Figure 17. First, average concentrations for each size bin were calculated for both the samples with the PCVI flows on and with the PCVI flows off. From each of these, the transmission efficiency of each bin size was calculated by dividing the ratio of particles transmitted with PCVI flows on over those with PCVI flows off. The data were fitted with a sigmoidal fit and the D50 was the particle diameter size that corresponded to a 50% transmission efficiency on the sigmoid. Based on the literature, the expected D50 for these flows was between 2.7 to 4 μm . The D50 calculated from this experiment is consistent within this range.

The PSL experiment was repeated three times over the course of two days. The results from one of the three experiments can be summarized in Figure 18. Figure 18A shows the mean particle concentration when the PCVI flows were off. Figure 18B shows the mean concentration of particles when the PCVI flows were on. When this experiment was repeated, similar results were found.

In all three experiments, there is a notable peak in the bins surrounding the 5 μm particle diameter. A similar analysis was performed on these measurements to determine the D50. The transmission efficiency was calculated for each size bin and then a sigmoid was fit to the data. The D50 calculated from these experiments ranged from 2.7-3.8 μm , though this is not a perfect measurement of D50 as the particle concentrations are skewed toward larger particle sizes since there is a high concentration of 5 μm particles.

5.4.3. Summary of PCVI Results

Overall, the PCVI is operating as intended. The D50 appears to be slightly larger than the expected theoretical value. This could be due to deviations in achieved versus intended flow rates. It could also be the result of inconsistencies in overall ambient particle concentrations in the air.

In order to refine the operating D50 of the PCVI, a more rigorous setup should be applied. A more steady concentration of particles, such as the setup described by Koolik (2016), could minimize fluctuations in particle size concentrations over time. Similarly, a controlled and consistent particle solution and generation would also improve the results of these tests.

In all, the PCVI tests proved that the PCVI is effective at segregating large particles from smaller ones. The PCVI has been tested extensively in Boulter et al. (2006), Kulkarni et al. (2011), and Koolik (2016), so these tests described are sufficient to determine that the PCVI within the SPIDER setup is functional.

5.5. Flow Verifications

The final verification tests for SPIDER ensured that all of the components were able to function together. Because the functionality of each of the three components is very flow-dependent, it is critical to verify that there is no flow blockage or clogging when the L-PCVI, chamber, and PCVI were connected in series and turned on.

In doing this, a recommended start-up sequence for SPIDER was established. The approach to starting up SPIDER while ensuring no flow blockage involves moving from the bottom-upwards. The first step is to connect all USB cables to ensure that the computer is able to

communicate with SPIDER. The critical communication lines are the Arduino, which transmits data from the temperature sensors; the Alicat, which controls and reports the flow values through each MFC; and any measurement devices such as an OPS, OPC, or mass spectrometer. Second, the vacuum pump and pressurized air should be turned on to provide flows to the MFCs. Next, the PCVI flows should be turned on by setting the AF followed by the PF. This will start a flow through the chamber. The last step is to turn on the flows for the L-PCVI, again turning on AF before PF. At each point in this process, the operator should pause and verify via pressure measurements or by checking the achieved flow rates that no flow problems have occurred.

A test was done to turn on SPIDER via the established protocol, and it verified that all of the individual components run in series without any flow problems. Between each flow change, the system was observed to verify that individual components were working. First, the flows into the OPS were started to see the ambient aerosol distribution in the room. After turning on the flows for the PCVI, the setup was left for five minutes to see if the PCVI was collecting only the particles larger than the D50. Once it was verified that this was the case, the flows for the L-PCVI were turned on. During this process, no blockage or clogging occurred anywhere in the setup. At this point, the IF of the L-PCVI was connected to the omni-directional inlet to sample from a cloud.

With this test, it was shown that the individual components are able to operate in series under the specific flows described in Table 4. To understand the flexibility of the flows capable of working in SPIDER, a test was done to verify that SPIDER is operational under varying flows into the L-PCVI. For this test, the PF was adjusted to different ratios of AF-to-IF ratios that matched the values in the literature (Hiranuma et al., 2016b).

Because the literature expresses the ratio of the two flows in LPM, this creates a slight difference to the AF-to-IF ratio discussed earlier. While the ratio of AF-to-IF for SPIDER's L-PCVI using SLPM for the flows is 0.19, the AF-to-IF ratio using LPM is 0.23. This difference arises because the conversion from LPM to SLPM is pressure and temperature dependent. The different flows within the L-PCVI do not have the same pressure and temperature, necessarily, so the ratio can change even though the flows in SLPM have not changed.

The different flows tested are summarized in Table 5. The AF and SF were held constant such that the PF directly influenced the IF and thus the AF-to-IF ratio. The secondary effect of this was that the changes in PF did not affect the flows of the instruments downstream of the L-PCVI. There were no noticeable effects on the PCVI or chamber as a result of changes in the PF, nor was there any sign of flow blockage or pressure changes within SPIDER. This indicates that there is flexibility in setting the D50 of the L-PCVI, as long as the SF stays constant. In future laboratory studies, this test should be performed with a constant input so that the outputs of the L-PCVI and PCVI can be directly compared.

6. Mount Washington Observatory Field Campaign

In April 2017, SPIDER was deployed at the summit of Mount Washington in New Hampshire. The field campaign took place over two weeks, during which SPIDER was operated for approximately eight days. The two goals of this campaign were to provide a proof of principle and to demonstrate that SPIDER can survive harsh weather conditions.

6.1. Mount Washington Observatory Field Site

Mount Washington (44°16'N, 71°18'W, 1914 m ASL) is the highest peak in the Presidential Range in the northern Appalachian Mountains (Seidel et al., 2007, 2009). Mt. Washington is surrounded by other rocky mountains that are part of the White Mountains and the Presidential Range. The summit sits slightly above the regional atmospheric mixing level of 1100-1500 m ASL, so the winds passing directly above the summit have been described as geostrophic in nature (Seidel et al., 2009). Additionally, Mt. Washington is affected by distinct air masses: continental polar, maritime polar, and maritime tropical (Murray et al., 2013). As a result, the mountain is known to experience extreme weather (<https://www.mountwashington.org/>).

This site provided a good location for testing SPIDER because of the known high prevalence of cloud cover and extreme weather. There are estimates of cloud cover, which range from full summit coverage during 51% of summer days (Murray et al., 2013; Seidel et al., 2007) to partial cloud or fog coverage during at least 300 days of the year (Smith, 1982). Additionally, strong winds provided a good test of the durability of SPIDER. The mean hourly wind speed at the summit is approximately 35 mph, and the observatory has been known to have a number of “century days” per year during which wind gusts are stronger than 100 mph (Smith, 1982). Further, a 231 mph wind was recorded at the summit on April 12, 1934, becoming the highest wind ever recorded on Earth (Smith, 1982).

At the summit of the mountain is the Mount Washington Observatory (MWO). The MWO opened in 1932 and has been operational, obtaining hourly weather measurements since then (Smith, 1982). Since opening, there have been a number of research projects done at MWO, including a rotating multi-cylinder, which was able to extract the liquid water content of supercooled clouds (Smith, 1982). There have also been a number of collaborations between MWO and MIT.

The equipment was set up in the server room at MWO. The server room had an exterior window that led to the “catwalk.” For 24 hours of measurements, SPIDER was located on the catwalk, with data transmitted via cables through the window. For all successive measurements, SPIDER was brought into the server room with a tube through the window connecting to an omni-directional inlet above the catwalk. The catwalk provided a good location for SPIDER since it was partially shielded on two sides from falling ice debris and extreme winds but still exposed to clouds.

6.2. Durability and Deployability

The primary objective of the proof-of-concept campaign was to deploy SPIDER to demonstrate its capability as a field instrument. This was performed in two distinct phases: transportation and deployment. Transportation was to and from MIT as well as up the steep, snow-covered mountain path. Once at MWO, SPIDER was then deployed for approximately

eight days, during which it was exposed to harsh winds and riming ice. In both of these phases, SPIDER proved to be resilient.

6.2.1. Transportation

Before leaving for MWO, the design proved to be effective at easing the preparation process. SPIDER is designed to have two modules that are easily separated and re-attached. This allows SPIDER to be carried in two smaller, easier to carry parts. Additionally, the bottom module of SPIDER rests on casters, which facilitated travel between vehicles. Once the modules were separated, they were covered by plastic wrap to prevent any scratches and to absorb some of the impact of driving over rough roads. Because the chiller is also easily detachable, it was transported as a separate piece. The cooling fluid was transported separately to prevent spillage. The support arms were also removed from SPIDER to allow it to lay as flat as possible.

A few lessons for future modifications were learned in the preparation phase. First, the current chiller is slightly too large for easy transportation. The current chiller weighs approximately 100 kg, requiring multiple people to lift it from vehicle to vehicle. Future field studies should seek a chiller equally as powerful at a smaller size. Second, plastic wrap was effective at preventing damage, but it would be wise to invest in a sturdier transportation case or other protective equipment for transportation.

In neither the drive to nor from the base of Mt. Washington did SPIDER incur any damage. All the pieces of SPIDER plus other gear for the campaign were driven in a large van. With the parts of SPIDER described in Chapter 4 were also a computer, various tools, and a few other instruments. Loading and unloading the van took approximately fifteen minutes each. The same was true for the ride back to MIT.

6.2.2. Deployment

Once at MWO, SPIDER was first deployed on April 15, 2017. It was secured with additional plastic wrap and tape to prevent any moisture from damaging electronics. For the first day of measurements, SPIDER was placed outside for approximately 24 hours. This placement exposed it fully to the harsh winds, rain, and riming. Conditions on the mountain during SPIDER's time outside included average winds of approximately 50 mph and a light drizzle. The maximum wind gust that SPIDER was exposed to was 97 mph.

After 24 hours outside, SPIDER suffered only very minor damages. One of the straps holding SPIDER to the ground had flown up and ripped a hole in the plastic wrap. Because the plastic wrap was punctured, some water was able to get into SPIDER without any damage done to the electronics. Future improvements to SPIDER should include making SPIDER more watertight.

To avoid any more serious damage early in the campaign, SPIDER was brought back inside. The inlet of the L-PCVI was connected to a long tube that stuck out of the window so that the omni-directional inlet could still sample from clouds that passed over. Over the next nine days, SPIDER ran from inside.

It is worth noting the success and durability of the plastic omni-directional inlet, the only 3D printed piece that was exposed to harsh environmental conditions over the entire eight day campaign. Over the course of the campaign, the omni-directional inlet rimed over with ice at least once per day. The inlet withstood days of being chipped at for ice removal. On the seventh day, a small piece of the inlet broke off due to excessive force when attempting to remove a very

thick piece of ice. This suggests that the 3D printed parts of SPIDER that will not be hammered or chipped at, such as the temperature sensor holders or brackets, should survive harsh conditions and extreme cold temperatures.

Overall, it is expected from these results that SPIDER should be able to withstand a field deployment. Because SPIDER survived the extreme weather of MWO with insignificant damage, it should be able to survive a typical field location.

6.3. Sample Verification Measurements

SPIDER collected measurements nearly continuously for ten days. At one-second resolution, this is over 800,000 data points in each of the OPCs, the OPS, and the temperature sensors. For the purposes of verifying SPIDER's efficacy as an instrument, an analysis of a few samples is sufficient rather than an analysis of the entire campaign.

A particularly moving story occurred on April 18, 2017. Between 11:30 AM and 1:30 PM, patches of frozen fog rolled over MWO, providing SPIDER with measurements in all three channels. When SPIDER samples directly from the frozen fog, there should be elevated counts of ice crystal residuals. In periods of less dense fog, there should be elevated levels of interstitial aerosol.

For these measurements, SPIDER was run with the flows summarized in Table 4. Figure 19 shows the resulting time series of the three channels plotted on the same time axis. To reduce noise, points in Figure 19A and 19B are displayed as the moving average over 30 seconds of measurements. The OPS provided much less noisy data, so it is plotted as raw concentration over time. The passing cloud is very visible in the interstitial aerosol measurement (Figure 19A). Here, there are a notable increases and decreases in interstitial aerosol as clouds pass by.

The trend is slightly less clear in Figure 19B and 19C. Freezing fog, as a descriptive weather term, refers to clouds made up of supercooled droplets that freeze on contact. Thus, it is expected that there should be a large number of supercooled droplets and some ice residuals within the fog. In the droplet residual channel, there is a constant signal with much smaller fluctuations. This is to be expected within a fog mass, with fluctuations only due to relative concentrations of droplets that go with changes in fog density.

There were only a few distinct hits of ice crystal residuals. This is appropriate for the weather conditions and expected natural abundance of INPs. The peaks in ice residuals typically line up with periods that the interstitial record suggests is more dense fog. In only one case does the INP arrive with a high concentration of interstitial aerosol at approximately 500 seconds. In this case, the INP arrives as the concentration of interstitial aerosol begins decreasing, potentially signifying the beginning of the patch of dense fog.

Overall, an analysis of this period suggests that SPIDER is capable of segregating out different cloud particle types. Future work should be done in analyzing a larger number of samples from this campaign to find other examples of successful measurements.

7. Summary and Future Work

This work introduced SPIDER, a new inlet for comprehensive studies of mixed-phase clouds. I will now conclude by providing an analysis of performance, a few suggestions for upgrades, and a couple recommended field locations.

7.1. Analysis of Performance

The verification and field deployment proved that both the individual components of SPIDER worked in their intended purposes and that the entire system functioned when these components were connected in series and operated on a mountain top campaign site.

In the verification measurements, each component of SPIDER was isolated and tested to ensure that it would perform its role in the overall system. The first measurements started from the top and worked down the instrument to make sure each piece functioned: first the L-PCVI, then the temperature controls, then the chamber, and finally the PCVI. Once each was verified individually, a test was done to ensure that the combination of instruments provided no problems in terms of flow blockage.

The L-PCVI measurements verified that the 3D-printed version of the IS-PCVI, as described by Hiranuma et al. (2016), is capable of achieving similar D50s. Two measurements were taken. First, it was proven that the D50 for the flow regime used in SPIDER's operation is larger than 10 μm . Second, it was shown that the D50 for a flow regime described by Hiranuma et al. (2016) has D50 smaller than approximately 38 μm . From these measurements it can be concluded that the printed L-PCVI using the flow regime for SPIDER will achieve a D50 similar to that theorized by the literature. Future experiments should be done to fully characterize the L-PCVI similar to the work in Koolik (2016). A full characterization of the L-PCVI would define the flow rates for obtaining the ideal D50 to segregate droplets and ice crystals from interstitial aerosol.

The temperature calibrations helped demonstrate the chamber response to changes in set temperature while simultaneously pointing to important improvements that must be made. These tests highlighted a few important successes and accomplishments. First, the temperature sensors are able to communicate with the computer at over a sample per second. Second, the temperature reported by the sensor is calibrated to the temperature sensor of the chiller, and thus the temperatures reported should be accurate. Finally, the measurements demonstrated that the chiller must be set between -40 and -50°C in order to achieve the -16°C required by WBF to evaporate droplets while sustaining ice crystals. An important conclusion from this work is that insulation must be greatly improved.

Tests on the chamber were important to verify that WBF process can sustain ice crystals while evaporating droplets using the residence time and temperature in the chamber. By running evaporation models to verify droplet evaporation, it is expected that droplets as large as 50 μm will evaporate given an expected supersaturation of 0.5 or below within the chamber. Given that 50 μm is probably larger than the expected droplet size entering the chamber, it is expected that droplets should fully evaporate within the chamber. By performing a test in which droplets were frozen homogeneously, it is shown that the chamber can sustain ice crystals. Together, the evaporation of droplets and not ice crystals shows that the chamber in SPIDER is operated under ideal conditions to see the effects of WBF. In the future, it would be beneficial to perform laboratory experiments on droplet evaporation.

Finally, the PCVI was tested to verify that its expected D50 was similar to the measured D50. By performing tests with both ambient air and 5 μm PSL particles, the range of D50s for the PCVI was found to be between 2.7-3.8 μm , slightly higher than the expected value. Still, the ice crystals as they enter the PCVI should be larger than this cut size based on the verification test to sustain ice crystals. Thus, the PCVI is operating with flows that make it effective at segregating ice crystals from droplet residuals.

After each component was verified individually, a test was done to put them all together in series and verify there are no flow issues preventing SPIDER from working. There were no problems experienced when firing up SPIDER or when the PF of the L-PCVI was adjusted while connected to the other parts. This demonstrates that SPIDER works as a combination of the instruments and that it has flexibility to change L-PCVI cut size without disrupting the other instruments.

SPIDER was also brought to MWO in New Hampshire where it proved its capability as a field instrument. As part of the proof-of-principle campaign, SPIDER verified that it can be transported to remote field locations, that it can withstand extreme weather, and that it can segregate interstitial aerosol, water droplets, and ice crystals. After the difficult journey to and from MWO and eight days of measurements, SPIDER returned to MIT without any damage and with over two million measurements for future analysis.

7.2. Future Improvements

The verification measurements and field campaign pointed out potential areas for improvement. While SPIDER works in its current configuration, there are a few improvements and updates that should be done before the next field campaign.

First, work should be done to better water-proof the lower module of SPIDER. This module houses all of the electronics for the instrument, so it is critical that it stay dry. Currently, the module is covered by six pieces of acrylic that have been cut to shape. This still leaves small but significant gaps that could introduce moisture into the system.

Second, the thermal insulation needs to be greatly improved. In the current setup, the chiller needs to be set between -40 to -50°C in order for the chamber to reach its desired temperature of -16°C. This can introduce the possibility of homogeneous freezing of droplets. Instead, better insulation should be added to the chamber to prevent heat exchange with the surroundings. After improving the insulation, the chamber response calibration should be repeated to derive a new cooling curve that shows the achieved chamber temperature as a function of set temperature.

There are two changes to the chamber that could improve its resistance to heat exchange. First, it could be greatly improved by switching the chamber to a double jacket chamber. By introducing a vacuum layer between the cooling fluid and the outside, heat exchange with the outside will be greatly reduced. Second, the new chamber should be cooled from the top to the bottom. The current chamber does not have cooling at the top and bottom 10 cm.

Another way the chamber could potentially improve would be to add a thin layer of ice to the walls instead of just having them be cold. Because the vapor pressure at the walls would thus be the saturation vapor pressure of ice at that temperature, the chamber would be guaranteed to be supersaturated with respect to ice, ensuring that the WBF process is active.

Finally, it would be beneficial to control the temperatures of the omni-directional inlet, L-PCVI and PCVI. With the omni-directional inlet, it would improve the system if the inlet was heated. This would prevent riming that causes flow choking. Because SPIDER requires an IF of

approximately 40 SLPM, it is critical that the cross-sectional area of the opening of the omnidirectional inlet is large enough for sufficient air to enter. This proved to be an issue during overnight measurements at MWO, as the omnidirectional inlet would freeze over during the cold nights. The L-PCVI could also be heated to prevent any freezing of supercooled droplets that impact against the sides.

Finally, pressure and relative humidity sensors should be installed at various points to increase the amount of information about the conditions occurring in SPIDER. Pressure sensors should be placed up- and down-stream of both the L-PCVI and PCVI. This will provide information about any clogging or choking of the flows. Additionally, relative humidity sensors should be placed above and below the chamber. This would help verify the evaporation model.

7.3. Future Field Studies

After the improvements suggested above are implemented, SPIDER should be brought out to the field to be used to study mixed-phase clouds in situ. There are a number of field sites that could provide useful information to the scientific community about mixed-phase clouds that would be good candidates for future SPIDER field campaigns.

First, it could be beneficial to return SPIDER to MWO for another, longer campaign. Because MWO has partial to full cloud cover 300 days of the year, it is an excellent site for studying clouds. A longer campaign during colder months could provide information about the composition of clouds that pass over the Appalachian Mountains.

Additionally, research at another field site in the United States could provide helpful information about cloud formation in the United States. Storm Peak Laboratory in the Rocky Mountains (40.45°N, 106.74 °W, 3210 m ASL) was built in the summer of 1995 and is managed by the Desert Research Institute (Borys and Wetzol, 1997). A number of field campaigns have been performed at Storm Peak Laboratory, including a large number of studies on aerosols and clouds (see Obrist et al., 2008; Hallar et al., 2013; Samburova et al., 2013; etc.). Combining the results from Storm Peak Laboratory with those from MWO could also provide important information about how aerosol populations develop as they cross the United States.

Another interesting field site would be the Sphinx Laboratory at Jungfraujoch (46°32'N, 7°59'E, 3580 m ASL) in the Swiss Alps (Kamphus et al., 2010). Jungfraujoch has been used in a number of studies on mixed-phase clouds because it is frequently surrounded by mixed-phase clouds. This site has a slightly smaller fraction of days with cloud cover, but it is known for mixed-phase clouds which makes it a perfect candidate for a field study with SPIDER.

Additionally, other instruments for studying clouds have been deployed here (see Verheggen et al., 2007; and Kamphus et al., 2010), so the results of the SPIDER campaign could be compared to pre-existing measurements in the literature.

Finally, it would be interesting to do a closure study on CCN and INP in North America by positioning three SPIDERS at different locations around the country. To track a single air mass as it moves west to east, the SPIDER network could include one on the west coast in Oregon, one at Storm Peak Laboratory in Colorado, and one at MWO. Coupled with chemical analysis of residuals, this could provide critical information about the composition of cloud-forming particles in North America.

7.4. Conclusions

The goal while designing SPIDER was to develop a comprehensive inlet for sampling and segregating different cloud particles. Through the verification tests and the field campaign, it

has been demonstrated that SPIDER is capable of sorting the three components of mixed-phase clouds into distinct channels.

The next step is to couple SPIDER with chemical analyzing instruments. Mass spectrometry, for example, can be used to determine the differences between the particles that nucleate ice and those that nucleate droplets in mixed-phase clouds. This work could have significant implications on modeling efforts, which have to make assumptions about cloud nucleation capabilities of various aerosols. With sufficient data, the results can be integrated into global climate models and used to understand the changing climate.

8. Acknowledgements

I would like to express the deepest gratitude for the opportunity to work on this project. The SPIDER project would not have been possible without the generous donation from Bill Martin. It was an absolute privilege to get to know you through this project. While your donation funded the project, your excitement for the work we did and your enthusiastic support of me really kept it going.

In both this work and in my career, I am indebted to Dr. Michael Roesch for his support, mentorship, and leadership in this project. Michael, thank you for teaching me everything I know about 3D printing, CVIs, mechanics, and design. You have truly made me into an engineer, and I would be lucky to have become even 10% the MacGyver you are.

I also offer my sincerest gratitude to my advisor Dr. Dan Cziczo without whom this project and degree would not have happened. Dan, thank you for your constant confidence and wisdom. I am so grateful to have had the opportunity to work in your research group.

I am also grateful to the entire Cziczo Group. Thank you for truly being a research family for me at MIT. I have learned so much from all of you, and I consider myself extremely lucky to have had the role models that I found in all of you. I owe my gratitude to Dr. Alexandria Johnson, Dr. Carolin Roesch, Dr. Sarvesh Garimella, Dr. Maria Zawadowicz, Martin Wolf, Lily Dove, Megan Godell, and Daisy Caban.

I would also like to express my appreciation to all of the faculty, research mentors, and staff who have supported and motivated me throughout my career at MIT. Specifically, I would like to thank Dr. Sam Bowring, Dr. Noelle Selin, Dr. Rebecca Saari, Dr. Sara Lance, Dr. Susan Solomon, and Dr. Claire Conceison, each of whom guided me through some part of my MIT career.

I also wish to thank my friends who have supported me throughout my MIT career. You each made these last four and a half years incredibly special. Listing all of you would make this section too long, so I would like to specifically thank Maranda Johnston, Ali Edwards, Gabriella del Hierro, Courtney Diamond, Caroline Walsh, Tori Jensen, Caitlin Cassidy, and Lee Bernick for their unconditional love and friendship throughout my career. I would also like to thank those of my non-MIT friends who have been there for me since before acceptance day. Bernardo Da Silva, Scott Shapiro, Keelin Severtson, and Hobie Hunter, thank you for the continued joy you have brought to my life, even from afar.

Last but not least, I would like to thank my family. I am so fortunate to have such a large and compassionate group of people supporting me. To all of my grandparents, uncles, aunts, and cousins, thank you for support and enthusiasm. To Juan, thank you for being my best friend and partner along my MIT journey. Sheina, thank you for keeping me in touch with what is cool and hip while I was stuck in the MIT bubble. Marissa, thank you for all of your edits to my work over my entire career and for reminding me that there is a whole world of academia that has nothing to do with math. To my mother, thank you for pushing me to go to MIT and for showing me how powerful, strong, and independent a woman can be. And last but not least, thank you to my father for the sense of humor and no-quitting attitude that was necessary to get me to where I am now.

9. References

Abel, S. J., Cotton, R. J., Barrett, P. A. and Vance, A. K.: A comparison of ice water content measurement techniques on the FAAM BAe-146 aircraft, *Atmos. Meas. Tech.*, 7, 3007–3022, doi:10.5194/amt-7-3007-2014, 2014.

Alicat Scientific: Technical Data for Alicat MC and MCR Mass Flow Controllers, , 30, 1–5, 2016.

Atkinson, J. D., Murray, B. J., Woodhouse, M. T., Whale, T. F., Baustian, K. J., Carslaw, K. S., Dobbie, S., O’Sullivan, D. and Malkin, T. L.: The Importance of Feldspar for Ice Nucleation by Mineral Dust in Mixed-Phase Clouds, *Nature*, 498, 355–358, 2013.

Bartolo, P. J., Ed.: *Stereolithography: Materials, Processes, and Applications*, illustrate., Springer Science & Business Media., 2011.

Baustian, K. J., Cziczo, D. J., Wise, M. E., Pratt, K. A., Kulkarni, G., Hallar, A. G. and Tolbert, M. A.: Importance of aerosol composition, mixing state, and morphology for heterogeneous ice nucleation: A combined field and laboratory approach, *J. Geophys. Res. Atmos.*, 117(6), 1–13, doi:10.1029/2011JD016784, 2012.

Bhushan, B. and Caspers, M.: An overview of additive manufacturing (3D printing) for microfabrication, *Microsyst. Technol.*, 23(4), 1117–1124, doi:10.1007/s00542-017-3342-8, 2017.

Borys, R. D. and Wetzel, M. A.: Storm Peak Laboratory: A Research, Teaching, and Service Facility for the Atmospheric Sciences, *Bull. Am. Meteorol. Soc.*, 78(10), 2115–2123, doi:10.1175/1520-0477(1997)078<2115:SPLART>2.0.CO;2, 1997.

Boucher, O., Randall, D., Artaxo, P., Bretherton, C., Feingold, G., Forster, P., Kerminen, V.-M., Kondo, Y., Liao, H., Lohmann, U., Rasch, P., Satheesh, S. K., Sherwood, S., Stevens, B. and Zhang, X.-Y.: Clouds and Aerosols, in *Climate Change 2013: The Physical Science Basis. Contribution of Working Group I to the Fifth Assessment Report of the Intergovernmental Panel on Climate Change*, pp. 571–657, Cambridge., 2013.

Boulter, J. E., Cziczo, D. J., Middlebrook, A. M., Thomson, D. S. and Murphy, D. M.: Design and Performance of a Pumped Counterflow Virtual Impactor, *Aerosol Sci. Technol.*, 40(11), 969–976, doi:10.1080/02786820600840984, 2006.

Dallas Semiconductor: DS18B20 Temperature Sensor. [online] Available from: <http://datasheets.maximintegrated.com/en/ds/DS18B20.pdf>, n.d.

Davis, S. M., Avallone, L. M., Weinstock, E. M., Twohy, C. H., Smith, J. B. and Kok, G. L.: Comparisons of in situ measurements of cirrus cloud ice water content, *J. Geophys. Res.*, 112, 1–15, 2007a.

Davis, S. M., Hallar, A. G., Avallone, L. M. and Engblom, W.: Measurement of Total Water with a Tunable Diode Laser Hygrometer : Inlet Analysis , Calibration Procedure , and Ice Water Content Determination, *Am. Meteorol. Soc.*, 463–475, doi:10.1175/JTECH1975.1, 2007b.

Formlabs: 3D Printing with Desktop Stereolithography: An Introduction for Professional Users.

[online] Available from: <http://formlabs.com/media/upload/Intro-sla-whitepaper-04.pdf>, 2015.

Friedman, B., Ardon-Dryer, K., Carrasquillo, A., Daumit, K., Boulanger, K., Cross, E., Browne, E., Kroll, J., Thornton, J. and Cziczo, D.: CCN closure and composition analysis of droplet-forming aerosol, *AIP Conf. Proc.*, 1527, 832–835, doi:10.1063/1.4803400, 2013.

Hagiwara, T.: Current Status and Future Prospects of Laser Stereolithography, *Proc SPIE*, 5662, 644–648, doi:10.1117/12.596757, 2004.

Hallar, A. G., Lowenthal, D. H., Clegg, S. L., Samburova, V., Taylor, N., Mazzoleni, L. R., Zielinska, B. K., Kristensen, T. B., Chirokova, G., McCubbin, I. B., Dodson, C. and Collins, D.: Chemical and hygroscopic properties of aerosol organics at Storm Peak Laboratory, *J. Geophys. Res. Atmos.*, 118(10), 4767–4779, doi:10.1002/jgrd.50373, 2013.

Hiranuma, N., Möhler, O., Kulkarni, G., Schnaiter, M., Vogt, S., Vochezer, P., Jarvinen, E., Wagner, R., Bell, D. M., Wilson, J., Zelenyuk, A. and Cziczo, D. J.: Development and characterization of an ice-selecting pumped counterflow virtual impactor (IS-PCVI) to study ice crystal residuals, *Atmos. Meas. Tech.*, 9, 3817–3836, doi:10.5194/amt-9-3817-2016, 2016a.

Hiranuma, N., Möhler, O., Kulkarni, G., Schnaiter, M., Vogt, S., Vochezer, P., Järvinen, E., Wagner, R., Bell, D. M., Wilson, J., Zelenyuk, A. and Cziczo, D. J.: Development and characterization of an ice-selecting pumped counterflow virtual impactor (IS-PCVI) to study ice crystal residuals, *Atmos. Meas. Tech.*, (April), 1–41, doi:10.5194/amt-2016-102, 2016b.

Hirst, E., Kaye, P. H., Greenaway, R. S., Field, P. and Johnson, D. W.: Discrimination of micrometre-sized ice and super-cooled droplets in mixed-phase cloud, *Atmos. Environ.*, 35, 33–47, 2001.

Hull, C. W.: Apparatus for production of three-dimensional objects by stereolithography, 1984.

Jacobs, P. F.: *Rapid Prototyping & Manufacturing: Fundamentals of StereoLithography*, 1st ed., Society of Manufacturing Engineers, Dearborn., 1992.

Kamphus, M., Etter-Mahl, M., Klimach, T., Drewnick, F., Keller, L., Cziczo, D. J., Mertes, S., Borrmann, S. and Curtius, J.: Chemical composition of ambient aerosol , ice residues and cloud droplet residues in mixed-phase clouds : single particle analysis during the Cloud and Aerosol Characterization Experiment, *Atmos. Chem. Phys.*, 10, 8077–8095, doi:10.5194/acp-10-8077-2010, 2010.

Kleinman, L. I., Daum, P. H., Lee, Y. N., Lewis, E. R., Sedlacek, A. J., Senum, G. I., Springston, S. R., Wang, J., Hubbe, J., Jayne, J., Min, Q., Yum, S. S. and Allen, G.: Aerosol concentration and size distribution measured below, in, and above cloud from the DOE G-1 during VOCALS-REx, *Atmos. Chem. Phys.*, 12(1), 207–223, doi:10.5194/acp-12-207-2012, 2012.

Koolik, L. P.: Characterization of a 3D Printed Pumped Counterflow Virtual Impactor and an Aerodynamic Lens Concentrator, Massachusetts Institute of Technology., 2016.

Korolev, A.: Limitations of the Wegener–Bergeron–Findeisen Mechanism in the Evolution of Mixed-Phase Clouds, *J. Atmos. Sci.*, 64, 3372–3375, doi:10.1175/JAS4035.1, 2007.

Korolev, A. V., Isaac, G. A., Cober, S. G., Strapp, J. W. and Hallett, J.: Microphysical characterization of mixed-phase clouds, *Q. J. R. Meteorol. Soc.*, 129, 39–65,

doi:10.1256/qj.01.204, 2003.

Korolev, A. V., Strapp, J. W., Isaac, G. A. and Nevzorov, A. N.: The Nevzorov Airborne Hot-Wire LWC – TWC Probe : Principle of Operation and Performance Characteristics, *Am. Meteorol. Soc.*, 1495–1510, 1998.

Kudelski, R., Cieslik, J., Kulpa, M., Dudek, P., Zagorski, K. and Rumin, R.: Comparison of Cost , Material and Time Usage in FDM and SLS 3D Printing Methods, *MEMSTECH*, 12–14, 2017.

Kuhn, T. and Heymsfield, A. J.: In Situ Balloon-Borne Ice Particle Imaging in High-Latitude Cirrus, *Pure Appl. Geophys.*, 173, 3065–3084, doi:10.1007/s00024-016-1324-x, 2016.

Kulkarni, G., Pekour, M., Afchine, A., Murphy, D. M. and Cziczo, D. J.: Comparison of Experimental and Numerical Studies of the Performance Characteristics of a Pumped Counterflow Virtual Impactor, *Aerosol Sci. Technol.*, 45(3), 382–392, doi:10.1080/02786826.2010.539291, 2011.

Kupiszewski, P., Weingartner, E., Vochezer, P., Schnaiter, M., Bigi, A., Gysel, M., Rosati, B., Toprak, E., Mertes, S. and Baltensperger, U.: The Ice Selective Inlet: A novel technique for exclusive extraction of pristine ice crystals in mixed-phase clouds, *Atmos. Meas. Tech.*, 8(8), 3087–3106, doi:10.5194/amt-8-3087-2015, 2015.

Larson, B. H. and Swanson, B. D.: Experimental investigation of the homogeneous freezing of aqueous ammonium sulfate droplets, *J. Phys. Chem. A*, 110(5), 1907–1916, doi:10.1021/jp054270l, 2006.

Lawson, R. P., Baker, B. A. and Schmitt, C. G.: An overview of microphysical properties of Arctic clouds observed in May and July 1998 during FIRE ACE top very high to 4000 L - •) concentrations of ice particles Arctic cirrus cloud was composed of very high concentrations of small ice, *J. Geophys. Res.*, 106(July 1998), 14989–15014, 2001.

Lin, H. and Heintzenberg, J.: A theoretical study of the counterflow virtual impactor, *J. Aerosol Sci.*, 26(6), 903–914, doi:10.1016/0021-8502(95)00024-7, 1995.

Lohmann, U. and Hoose, C.: Sensitivity studies of different aerosol indirect effects in mixed-phase clouds, *Atmos. Chem. Phys.*, 9, 8917–8934, 2009.

McCoy, D. T., Tan, I., Hartmann, D. L., Zelinka, M. D. and Storelvmo, T.: On the relationships among cloud cover, mixed-phase partitioning, and planetary albedo in GCMs, *J. Adv. Model. Earth Syst.*, 8, 650–668, doi:10.1002/2013MS000282.Received, 2016.

Mertes, S., Verheggen, B., Walter, S., Connolly, P. J., Ebert, M., Schneider, J., Bower, K. N., Cozic, J., Weinbruch, S., Baltensperger, U. and Weingartner, E.: Counterflow Virtual Impactor Based Collection of Small Ice Particles in Mixed-Phase Clouds for the Physico-Chemical Characterization of Tropospheric Ice Nuclei: Sampler Description and First Case Study, *Aerosol Sci. Technol.*, 41(9), 848–864, doi:10.1080/02786820701501881, 2007.

Murray, G. L. D., Kimball, K. D., Hill, L. B., Hislop, J. E. and Weathers, K. C.: Long-Term Trends in Cloud and Rain Chemistry on Mount Washington, New Hampshire, *Water Air Soil Pollut.*, 224(1653), 1–14, doi:10.1007/s11270-013-1653-7, 2013.

Myhre, G., Shindell, D., Bréon, F.-M., Collins, W., Fuglestad, J., Huang, J., Koch, D.,

- Lamarque, J.-F., Lee, D., Mendoza, B., Nakajima, T., Robock, A., Stephens, G., Takemura, T. and Zhang, H.: Anthropogenic and Natural Radiative Forcing, *Clim. Chang. 2013 Phys. Sci. Basis. Contrib. Work. Gr. I to Fifth Assess. Rep. Intergov. Panel Clim. Chang.*, 659–740, doi:10.1017/CBO9781107415324.018, 2013.
- Obrist, D., Hallar, A. G., McCubbin, I., Stephens, B. B. and Rahn, T.: Atmospheric mercury concentrations at Storm Peak Laboratory in the Rocky Mountains: Evidence for long-range transport from Asia, boundary layer contributions, and plant mercury uptake, *Atmos. Environ.*, 42(33), 7579–7589, doi:https://doi.org/10.1016/j.atmosenv.2008.06.051, 2008.
- Ogren, J. A., Heintzenberg, J. and Charlton, R. J.: In-Situ Sampling of Clouds with a Droplet to Aerosol Converter, *Geophys. Res. Lett.*, 12(3), 121–124, 1985.
- Patade, S., Shete, S., Malap, N., Kulkarni, G. and Prabha, T. V.: Observational and simulated cloud microphysical features of rain formation in the mixed phase clouds observed during CAIPEEX, *Atmos. Res.*, 169, 32–45, doi:10.1016/j.atmosres.2015.09.018, 2015.
- Pekour, M. S. and Cziczo, D. J.: Wake Capture, Particle Breakup, and Other Artifacts Associated with Counterflow Virtual Impaction, *Aerosol Sci. Technol.*, 45(6), 758–764, doi:10.1080/02786826.2011.558942, 2011.
- Pruppacher, H. R. and Klett, J. D.: *Microphysics of Clouds and Precipitation*, 2nd ed., Kluwer Academic Publishers, Dordrecht., 1997.
- Roesch, M., Roesch, C. and Cziczo, D. J.: Dry particle generation with a 3-D printed fluidized bed generator, *Atmos. Meas. Tech.*, 10, 1999–2007, 2017.
- Rogers, R. R. and Yau, M. K.: *A Short Course in Cloud Physics*, 3rd ed., Elsevier Science, Tarrytown., 1989.
- Samburova, V., Hallar, A. G., Mazzoleni, L. R., Saranjampour, P., Lowenthal, D., Kohl, S. D. and Zielinska, B.: Composition of water-soluble organic carbon in non-urban atmospheric aerosol collected at the Storm Peak Laboratory, *Environ. Chem.*, 10(5), 370–380 [online] Available from: <https://doi.org/10.1071/EN13079>, 2013.
- Seidel, T. M., Grant, A. N., Pszenny, A. A. P. and Allman, D. J.: Dewpoint and Humidity Measurements and Trends at the Summit of Mount Washington, New Hampshire, 1935 – 2004, *Am. Meteorol. Soc.*, 20, 5629–5641, doi:10.1175/2007JCLI1604.1, 2007.
- Seidel, T. M., Weihrauch, D. M., Kimball, K. D., Pszenny, A. A. P., Soboleski, R., Crete, E. and Murray, G.: Evidence of Climate Change Declines with Elevation Based on Temperature and Snow Records from 1930s to 2006 on Mount Washington, New Hampshire, Arctic, Antarct. Alp. Res., 41(3), 362–372, doi:10.1657/1938-4246-41.3.362, 2009.
- Shupe, M., Daniel, J. S., De Boer, G., Eloranta, E. W., Kollias, P., Long, C. N., Luke, E. P., Turner, D. D. and Verlinde, J.: A Focus on Mixed-Phase Clouds, *Am. Meteorol. Soc.*, 1549–1562, doi:10.1175/2008BAMS2378.1, 2008.
- Shupe, M. D., Matrosov, S. Y. and Uttal, T.: Arctic Mixed-Phase Cloud Properties Derived from Surface-Based Sensors at SHEBA, *Am. Meteorol. Soc.*, 697–711, 2006.
- Slowik, J. G., Cziczo, D. J. and Abbatt, J. P. D.: Analysis of cloud condensation nuclei

composition and growth kinetics using a pumped counterflow virtual impactor and aerosol mass spectrometer, *Atmos. Meas. Tech.*, 4(8), 1677–1688, doi:10.5194/amt-4-1677-2011, 2011.

Smith, A. A.: The Mount Washington Observatory - 50 Years Old, *Bull. Am. Meteorological Soc.*, 63(9), 986–995, 1982.

Storelvmo, T., Kristjansson, J. E. and Lohmann, U.: Aerosol Influence on Mixed-Phase Clouds in CAM-Oslo, *J. Atmos. Sci.*, 65, 3214–3230, doi:10.1175/2008JAS2430.1, 2008.

Strapp, J. W., Lilie, L. E., Ratvasky, T. P., Davison, C. and Dumont, C.: Isokinetic TWC Evaporator Probe: Development of the IKP2 and Performance Testing for the HAIC-HIWC Darwin 2014 and Cayenne-2015 Field Campaigns, *Am. Inst. Aeronaut. Astronaut.*, (June), 1–28, doi:10.2514/6.2016-4059, 2016.

TSI: Model 3330 Optical Particle Sizer Spectrometer., 2011.

Tsushima, Y., Emori, S., Ogura, T., Kimoto, M., Webb, M. J., Williams, K. D., Ringer, M. A., Soden, B. J., Li, B. and Andronova, N.: Importance of the mixed-phase cloud distribution in the control climate for assessing the response of clouds to carbon dioxide increase : a multi-model study, *Clim. Dyn.*, doi:10.1007/s00382-006-0127-7, 2006.

Verheggen, B., Cozic, J., Weingartner, E., Bower, K., Mertes, S., Connolly, P., Gallagher, M., Flynn, M., Choularton, T. and Baltensperger, U.: Aerosol partitioning between the interstitial and the condensed phase in mixed-phase clouds, *J. Geophys. Res.*, 112(1), 1–13, doi:10.1029/2007JD008714, 2007.

Verlinde, J., Harrington, J. Y., McFarquhar, G. M., Yannuzzi, V. T., Avramov, A., Greenberg, S., Johnson, N., Zhang, G., Poellot, M. R., Mather, J. H., Turner, E., Eloranta, E. W., Zak, B. D., Prenni, A. J., Daniel, J. S., Kok, G. L., Tobin, D. C., Holz, R., Sassen, K., Spangenberg, D., Minnis, P., Tooman, T. P., Ivey, M. D., Richardson, S. J., Bahrmann, C. P., Shupe, M., DeMott, P. J., Heymsfield, A. J. and Schofield, R.: The mixed-phase arctic cloud experiment, *Am. Meteorol. Soc.*, (July 2006), 205–221, doi:10.1175/BAMS-88-2-205, 2007.

Wang, B., Lambe, A. T., Massoli, P., Onasch, T. B., Davidovits, P., Worsnop, D. R. and Knopf, D. A.: The deposition ice nucleation and immersion freezing potential of amorphous secondary organic aerosol : Pathways for ice and mixed-phase cloud formation, *J. Geophys. Res.*, 117, 1–12, doi:10.1029/2012JD018063, 2012.

Wong, K. V and Hernandez, A.: A Review of Additive Manufacturing, *ISRN Mech. Eng.*, 2012, doi:10.5402/2012/208760, 2012.

10. Tables

Table 1: Summary of IWC, TWC, LWC Instruments

Instrument	Described By	Measures	Mechanism
Nevzorov Probe	Korolev et al. (1998)	LWC, TWC (IWC inferred)	Hot Wire Heat Transfer Calculations
IKP-2	Strapp et al. (2016)	TWC	Isokinetic Inlet and Hot Wire
CLH	Davis et al. (2007)	TWC (IWC can be calculated)	Subisokinetic Inlet and Evaporation
CPI	Lawson et al. (2001)	IWC and particle size distribution	High-resolution imaging

Table 2: Summary of CVIs

Instrument	Described By	Capability
CVI	Ogren et al. (1985)	Size-selects aerosol larger than a specified cut size using airflow from aircraft velocity
PCVI	Boulter et al. (2006)	Size-selects aerosol larger than a specified cut size using a vacuum pump
Ice-CVI	Mertes et al. (2007)	Separates ice crystals between 5-20 μm in diameter from droplets and interstitial aerosol
Ice Selective Inlet	Kupiszewski et al. (2015)	Separates ice crystals smaller than 20 μm in diameter from mixed-phase clouds
IS-PCVI	Hiranuma et al. (2016)	Size-selects for ice crystals larger than 10 μm in diameter
SPIDER	This work	Separates ice crystals, droplet residuals, and interstitial aerosol for simultaneous sampling

Table 3: Summary of Additive Manufacturing Techniques

Technique Name	Summary of Method	Cost	Resolution	Post-Processing
Selective Laser Sintering (“SLS”)	Binds powdered material together using a laser	High	Low	None
Fused Deposition Modeling (“FDM”)	Builds an object by depositing melted material	Low	Low	Low-Medium
Laminated Object Manufacturing (“LOM”)	Cuts thin sheets that have been joined together	Low	Low	None
Stereolithography Apparatus (“SLA”)	Selectively hardens a liquid resin using a laser.	Medium	High	Low

Table 4: SPIDER Flows

Component	L-PCVI			Chamber	PCVI		
	PF	AF	SF		PF	AF	SF
Flow (SLPM)	42.7	10	6.68	6.68	7.68	2	1

Table 5: L-PCVI Flow Tests

AF-to-IF Ratio	Flows (LPM)			
	AF	IF	PF	SF
0.14*	7	50	50.5	6.5
0.16	11.7	72.2	77.7	6.5
0.23	11.7	50.2	55.9	6.5

*Refers to the ratio and flows used by Hiranuma et al. (2016).

11. Figures

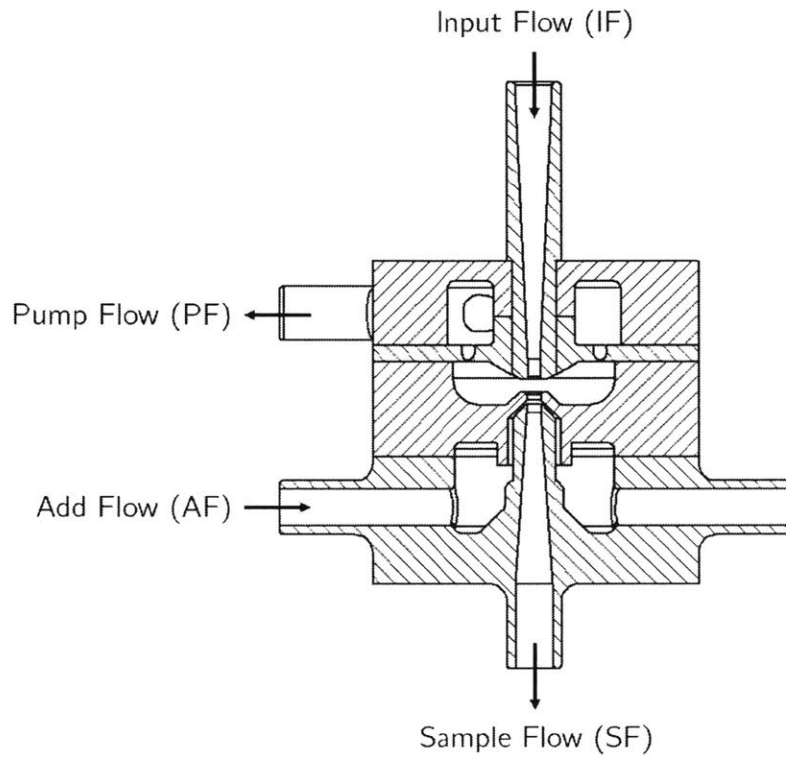


Figure 1. **Schematic of PCVI.** A cross-sectional view of the PCVI has the flows labeled for convenience. This PCVI is the 3D printed version, and it has incorporated a few of the suggestions from Kulkarni et al. (2011), including a slanted inlet nozzle.

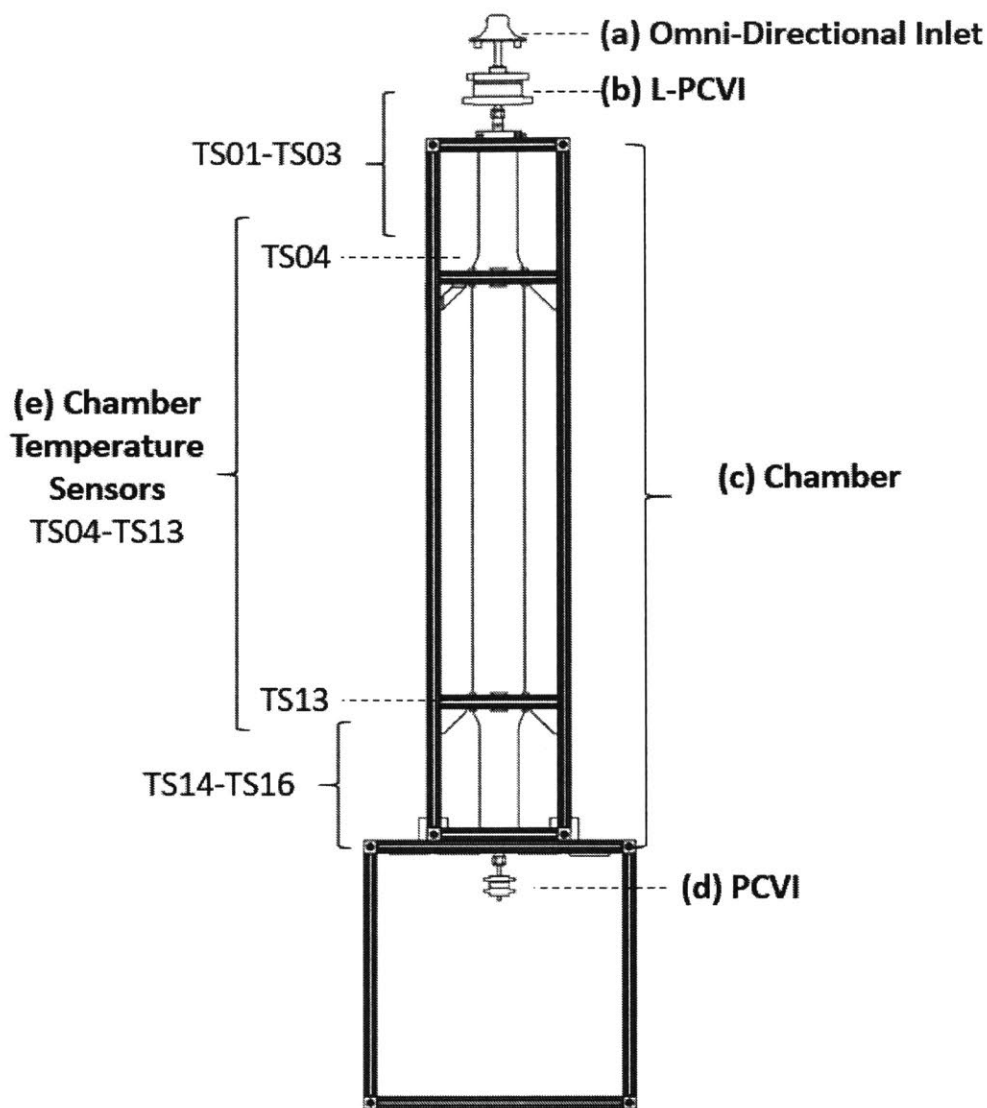


Figure 2. **Schematic of SPIDER.** A cartoon depiction of the new SPIDER inlet has its individual components labelled. (a) The omni-directional inlet prevents large rain droplets or other debris from entering SPIDER. (b) The L-PCVI is based on the designs by Hiranuma et al. (2016) and separates interstitial aerosol from the droplets and ice crystals. (c) The chamber is cooled to harness WBF process to evaporate droplets. (d) The PCVI downstream will separate evaporated droplet residuals from the ice crystals. (e) The chamber temperature sensors provide information about the achieved temperature in the chamber.

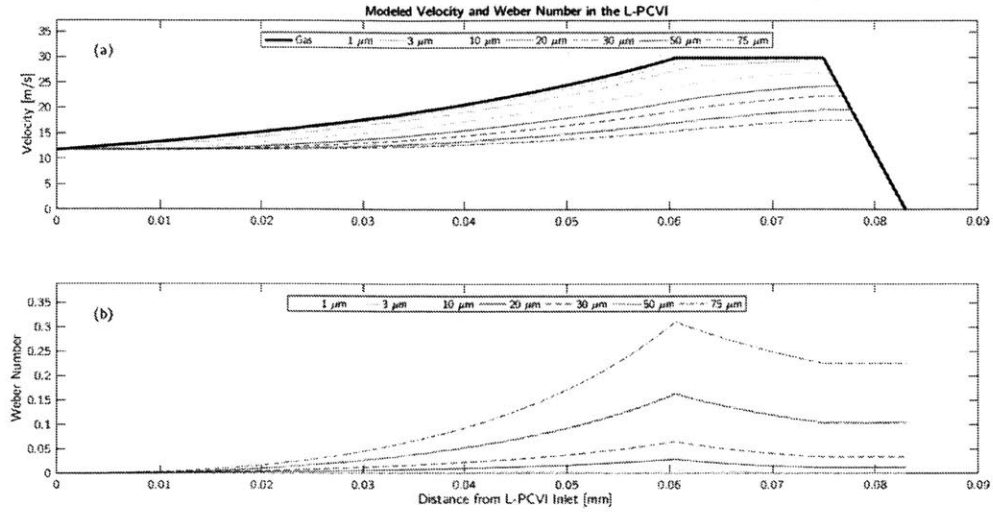


Figure 3. **Modeled Weber Number in the L-PCVI.** A model was run to calculate the velocity and Weber Number for droplets of varying sizes in the L-PCVI. (a) The velocity calculated for each droplet and the gas is shown as a function of distance from the inlet. (b) The Weber number was calculated at each point along the L-PCVI inlet.

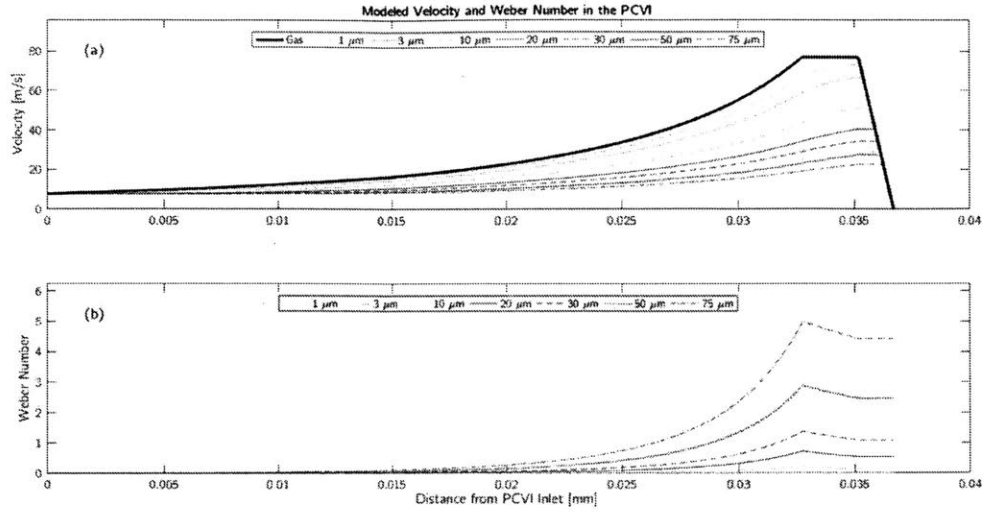


Figure 4. **Modeled Weber Number in the PCVI.** The same model was run to determine the velocity and Weber Number for droplets of varying sizes in the PCVI. (a) The velocity calculated for each droplet and the gas is shown as a function of distance from the inlet. (b) The Weber number at each point along the PCVI inlet.

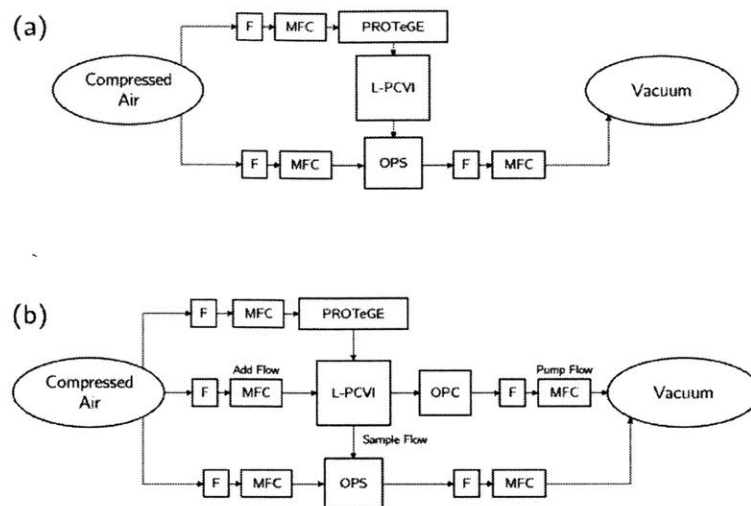


Figure 5. **Schematic of the L-PCVI Lower Bound Test.** To ensure that the D50 of the 3D printed LPCVI was larger than $10\text{ }\mu\text{m}$, this test was performed. (a) First, a standard of comparison was generated by running $10\text{ }\mu\text{m}$ PSL into the L-PCVI without the AF and PF of the L-PCVI on. (b) These flows were then turned on to see which residuals were able to pass through the stagnation plane.

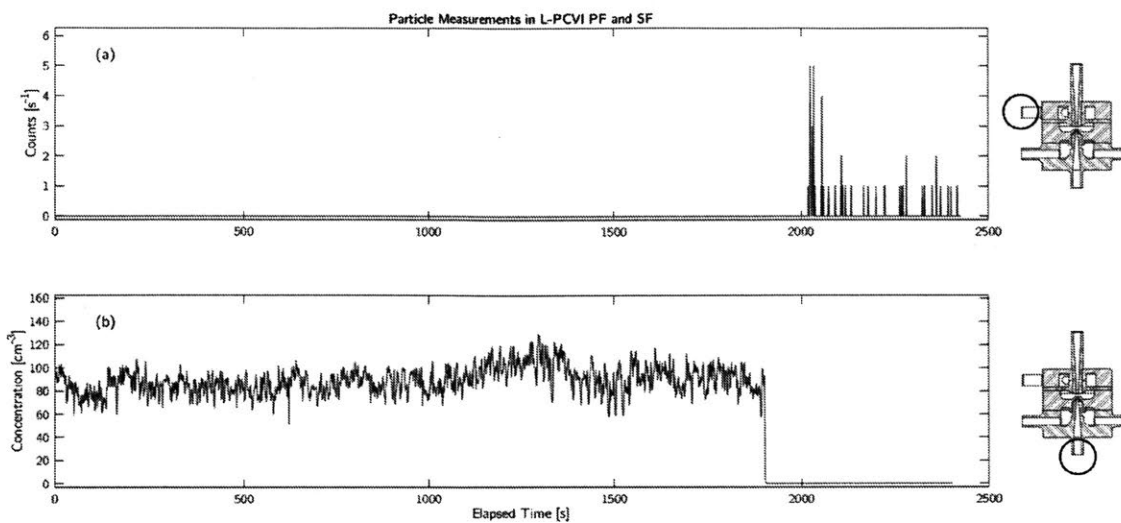


Figure 6. **Results of the L-PCVI Lower Bound Test.** Samples were collected in both the PF and SF of the L-PCVI. (a) The PF of the L-PCVI did not measure anything until the L-PCVI was turned on. (b) The SF of the L-PCVI saw a constant signal of large particles until the L-PCVI was turned on.

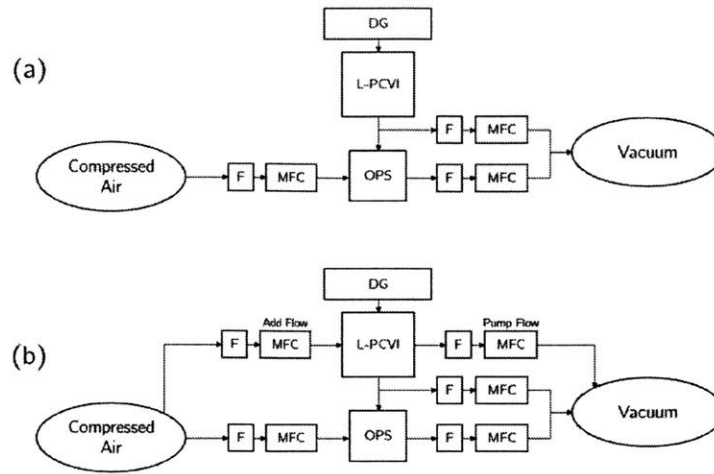


Figure 7. **Schematic of the L-PCVI Verification Test.** To verify that the 3D printed L-PCVI works as described by Hiranuma et al. (2016), a test was done using the flow values used by the literature. (a) The first measurement was performed without turning on the L-PCVI. (b) The second measurement used values for AF and PF found in the literature.

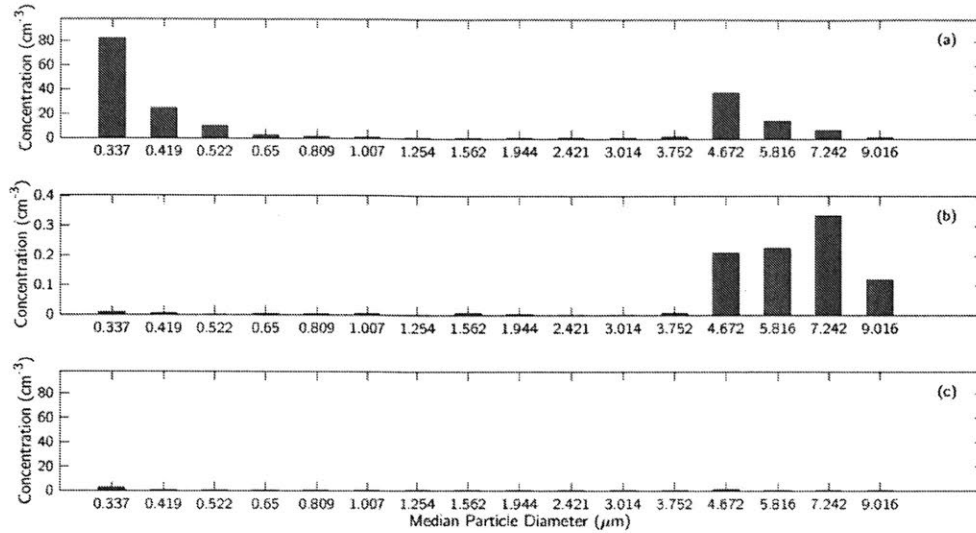


Figure 8. **Results of the L-PCVI Verification Test.** Three results from the L-PCVI verification test are demonstrated. (a) The L-PCVI off provides information about the input into the L-PCVI. (b) Once the AF and PF of the L-PCVI were turned on, there was a signal in the larger size range of the L-PCVI. (c) The L-PCVI was also operated with only the AF on to verify that L-PCVI works to reject droplets.

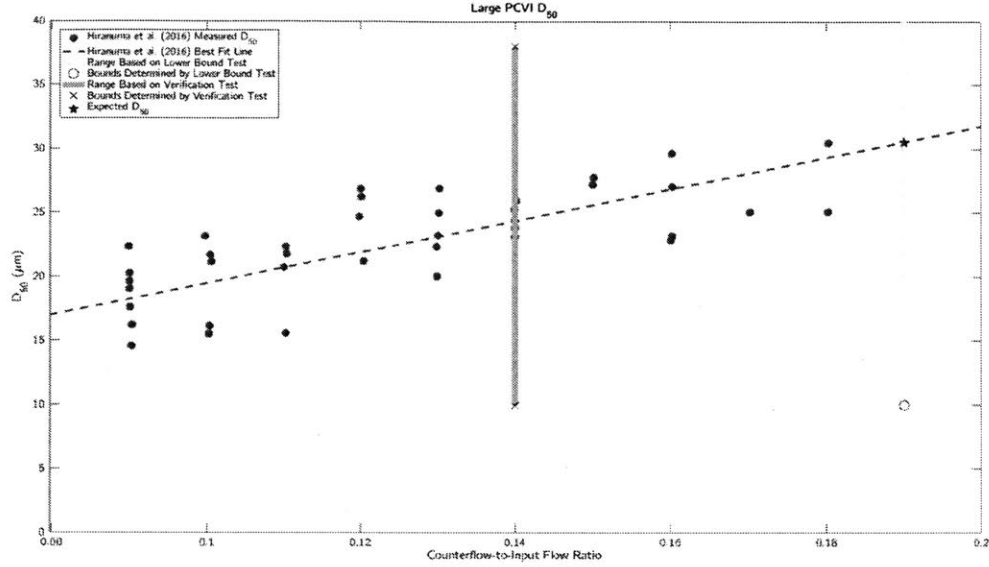


Figure 9. **Expected L-PCVI D50.** The results of this work are superimposed onto the data obtained in Hiranuma et al. (2016). Gray circles and the gray dashed line refer to the values from the literature. The “X” and “O” markers refer to data points obtained in measurements done in this work. The gray vertical lines indicate the ranges that were determined as part of this work. The red star is the anticipated D50 using SPIDER’s flow ratio.

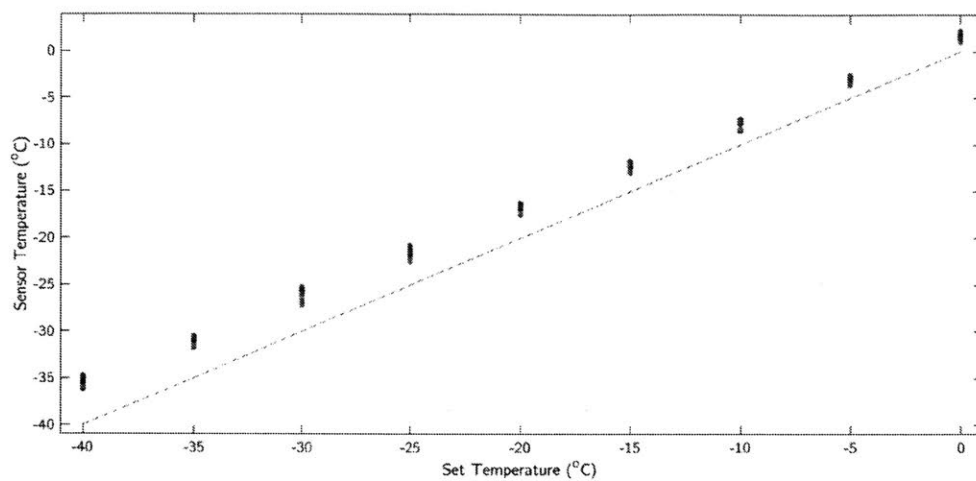


Figure 10. **Temperature Sensor Calibration.** The temperature sensors were calibrated by being submerged into the cooling fluid at a series of temperatures between 0 and -40°C. The dashed line depicts the ideal behavior where sensor readings match set temperature.

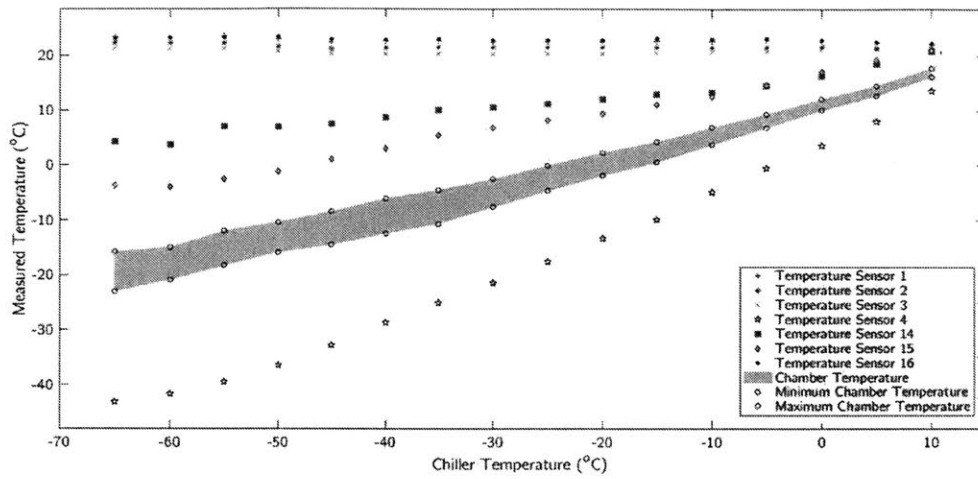


Figure 11. **SPIDER Temperature Response Curve.** The temperature achieved by each sensor as a response to the set temperature in the chiller. The shaded area represents the temperature achieved in the chamber temperature sensors, with the exception of sensor 4 which is shown as a small star.

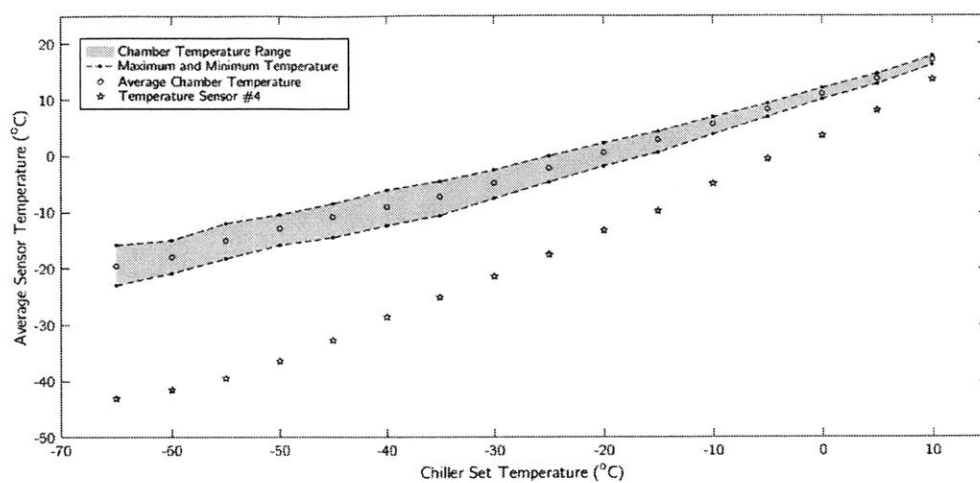


Figure 12. **Chamber Temperature Response Curve.** The temperature achieved in the chamber as a function of set temperature. Temperature sensor 4 is depicted alone because it is located directly at the fluid entry point and has a significantly colder temperature than the other sensors.

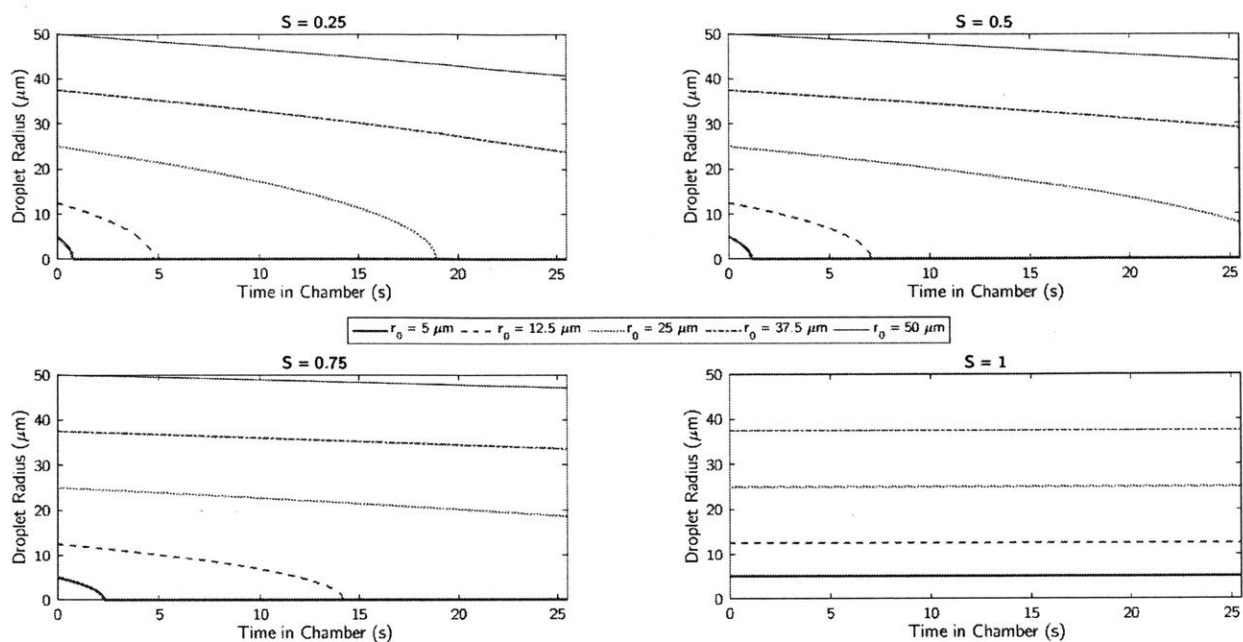


Figure 13. **Droplet Evaporation Model.** A droplet evaporation model was run under four levels of supersaturation for five different sized droplets.

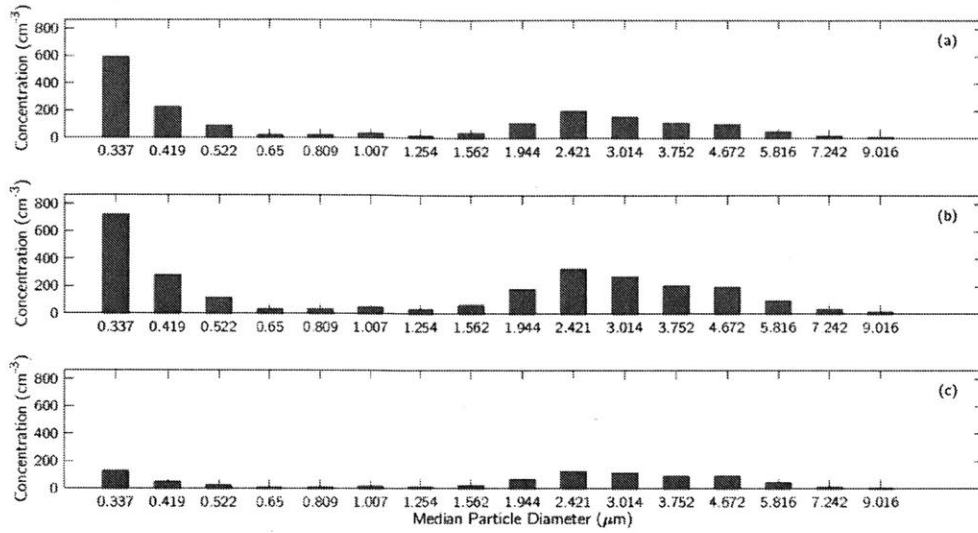


Figure 14. **Ice Crystal Measurement.** Droplets were homogeneously frozen and measured under three scenarios. (a) Ambient air was introduced to the cooled chamber with the PCVI on. (b) Droplets were introduced into the cooled chamber with the PCVI on. (c) The ambient air mean concentrations were subtracted from the mean concentrations of the droplets.

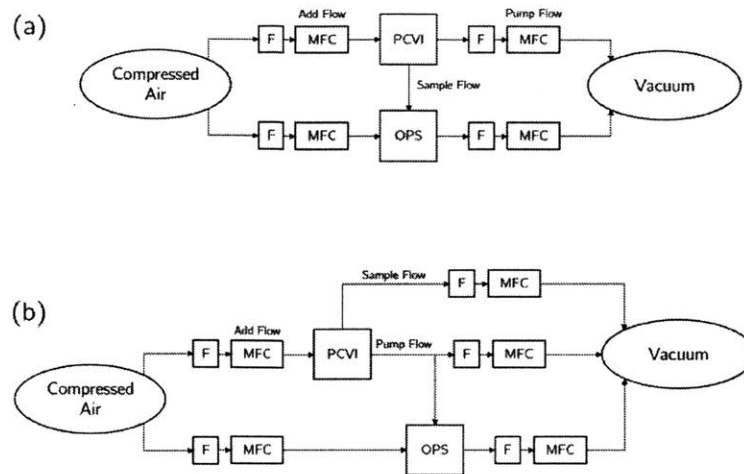


Figure 15. **Schematic of the PCVI Verification Measurements.** To verify the D50 of the PCVI, a few measurements were done. (a) The PCVI was turned off and on with the OPS in the SF. (b) The PCVI was turned on with the OPS in the PF.

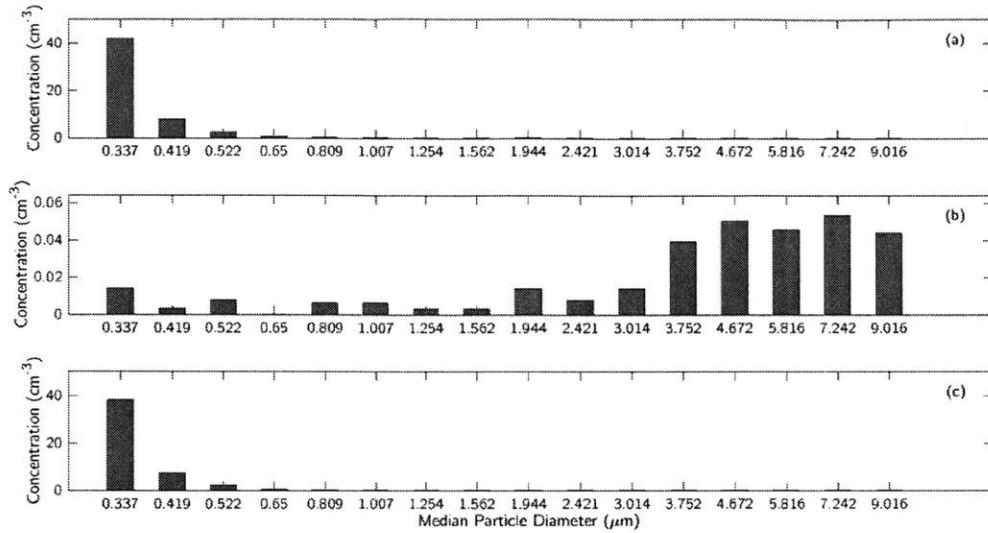


Figure 16. **Results of the PCVI Verification Measurements.** Three measurements are shown from the PCVI verification test. (a) The PCVI is turned off with the OPS in the SF. (b) The PCVI is turned on with the OPS in the SF. (c) The PCVI is turned on with the OPS in the PF.

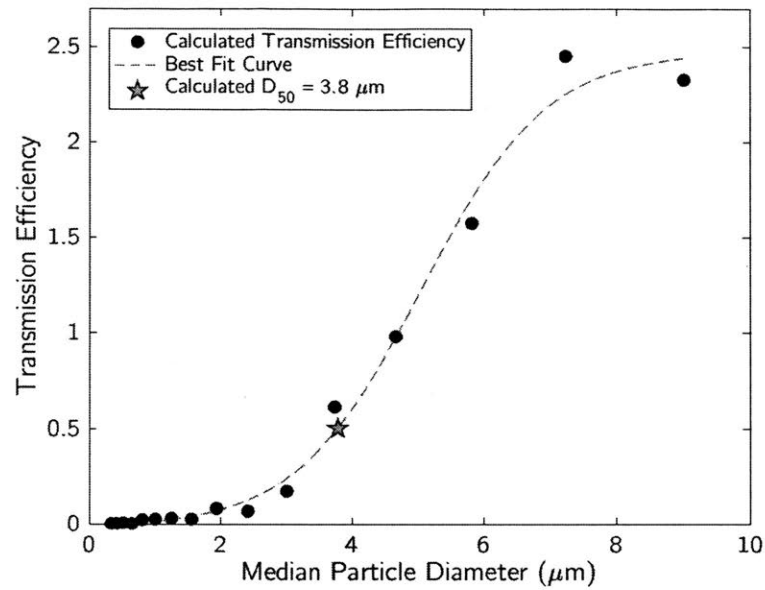


Figure 17. **Sample D50 Calculation Curve.** The transmission efficiency of each particle diameter was calculated and fitted with a sigmoidal curve. The star represents the particle size at which 50% of particles are transmitted.

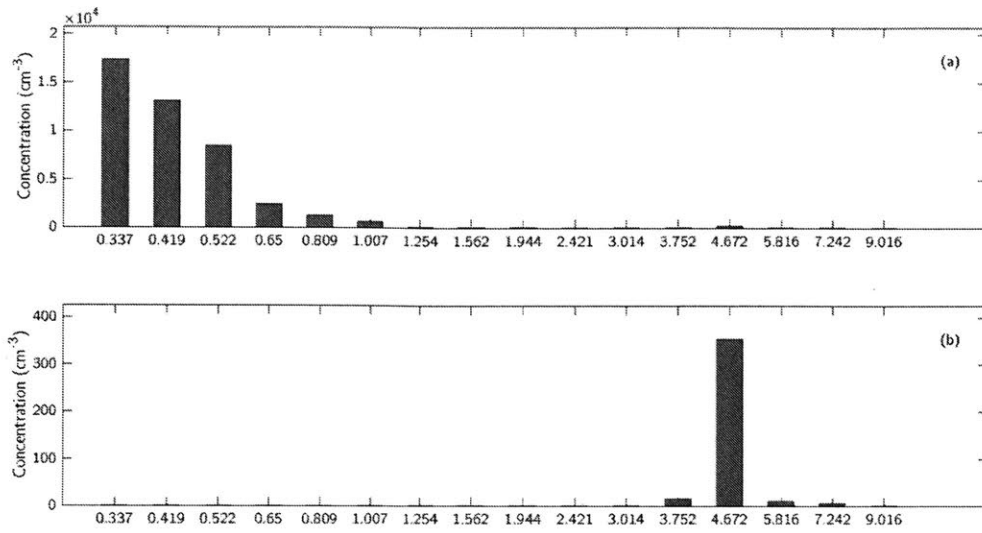


Figure 18. **Results of one PCVI PSL Measurement.** Verification measurements were performed using 5 μm PSL spheres. (a) The background concentration entering the PCVI. (b) The number concentration of particles transmitting through the PCVI when the flows are on.

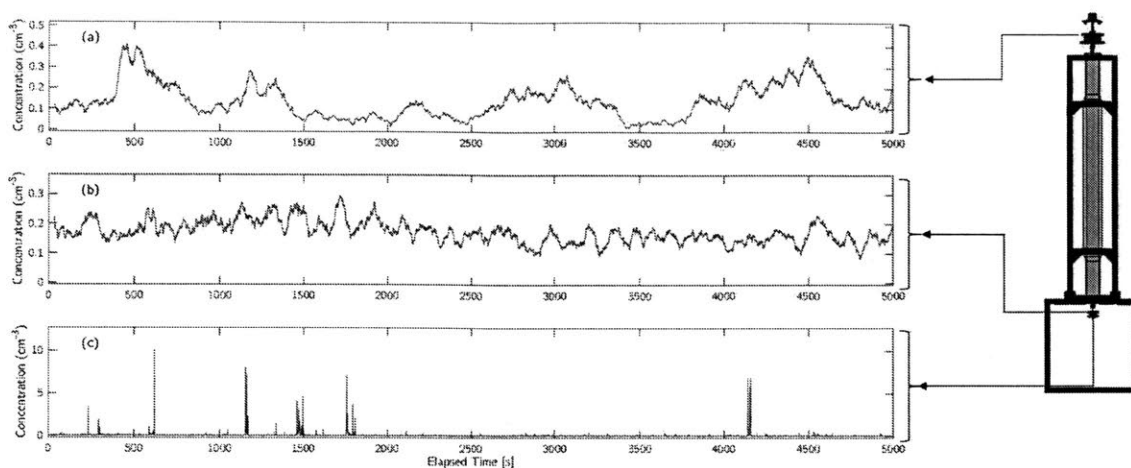
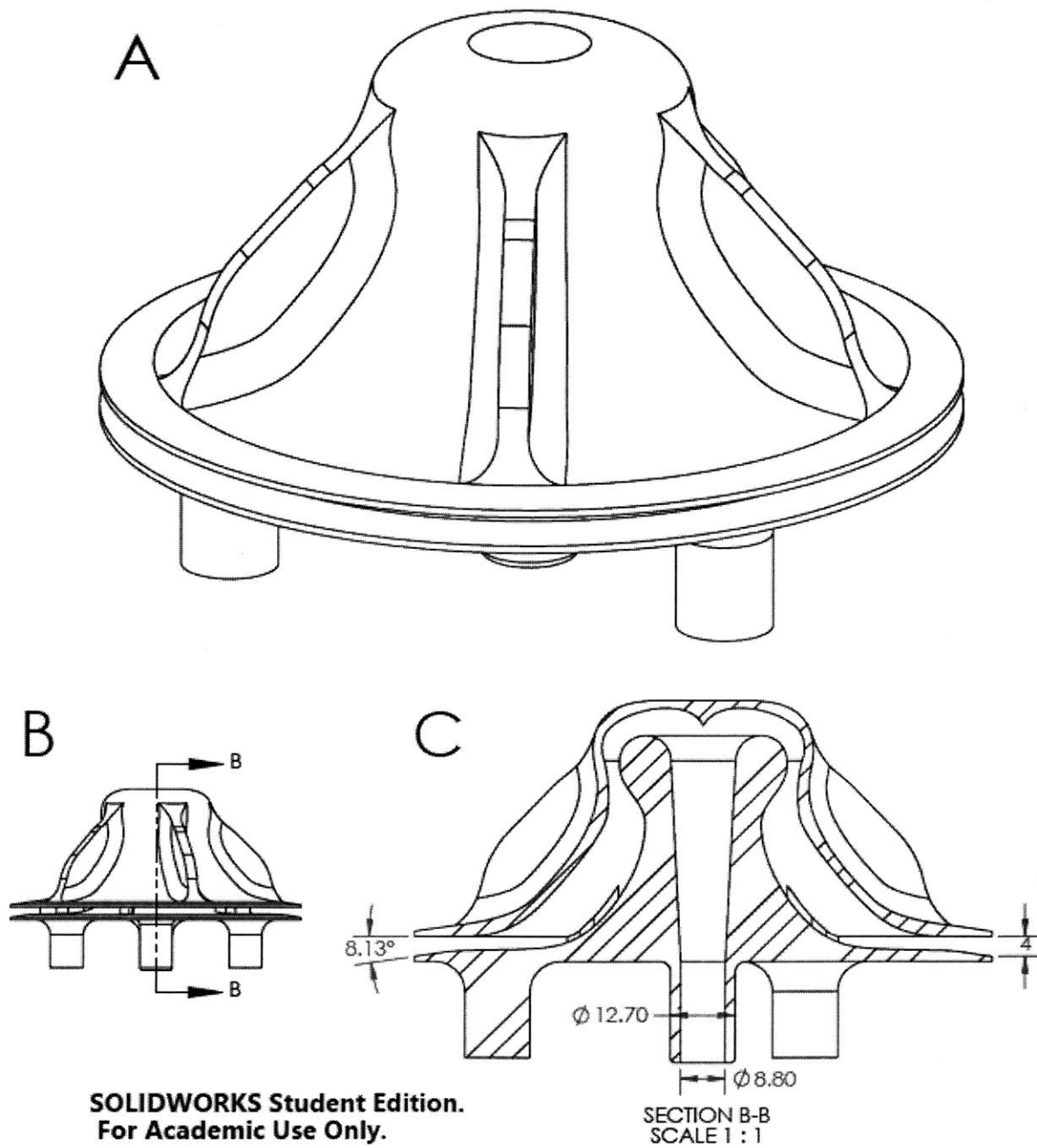


Figure 19. Sample Measurement from Mt. Washington. The results from the late morning of April 18, 2017 during which a frozen fog moved across the mountain summit. (a) The interstitial aerosol collected in the PF of the L-PCVI. (b) The droplet residuals that transmitted through the L-PCVI but were rejected in the PCVI. (c) The ice crystal residuals that were able to transmit through both the L-PCVI and the PCVI.

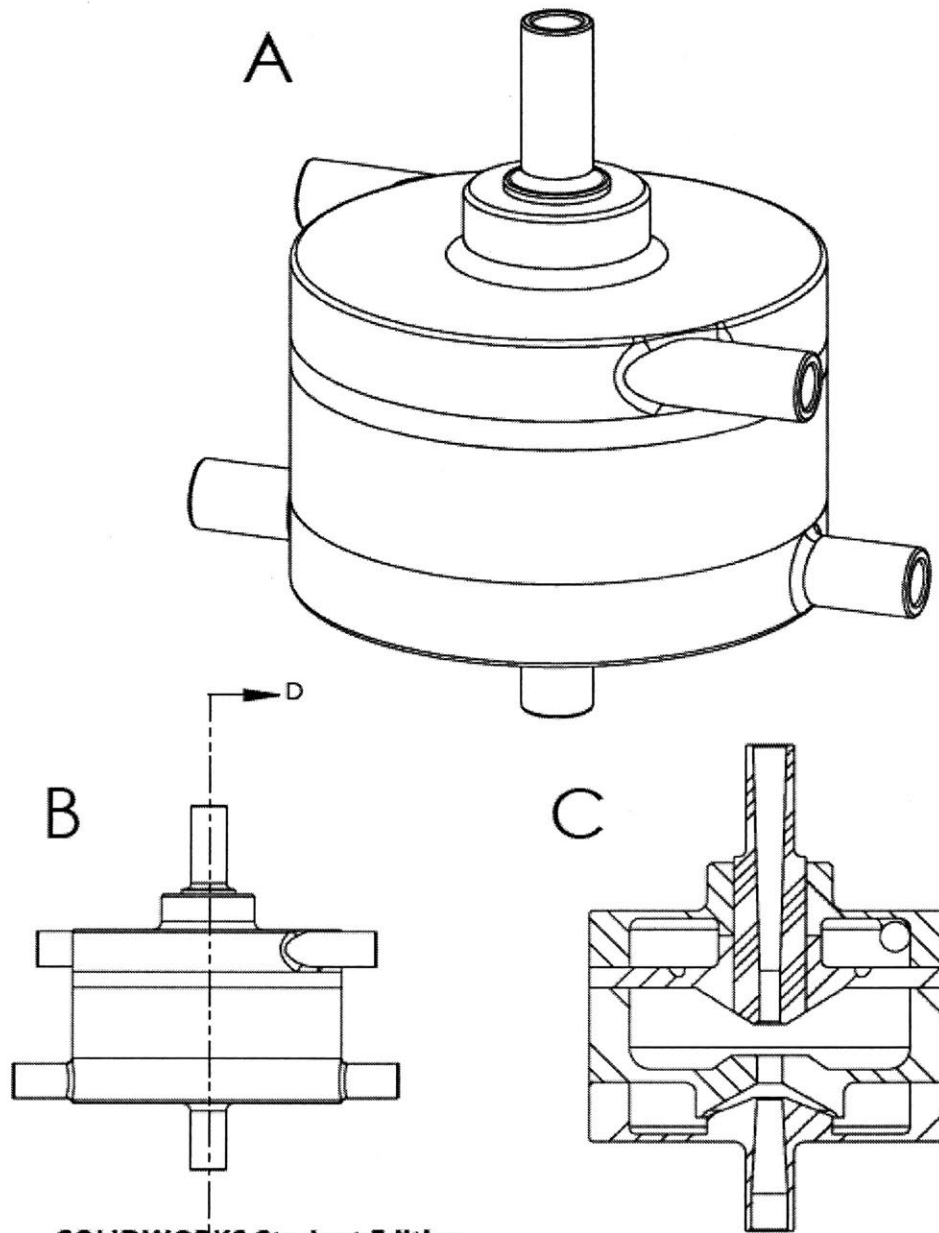
12. CAD Drawings

OMNI-DIRECTIONAL INLET



(C) KOOLIK AND ROESCH, 2017

LARGE PCVI (L-PCVI)



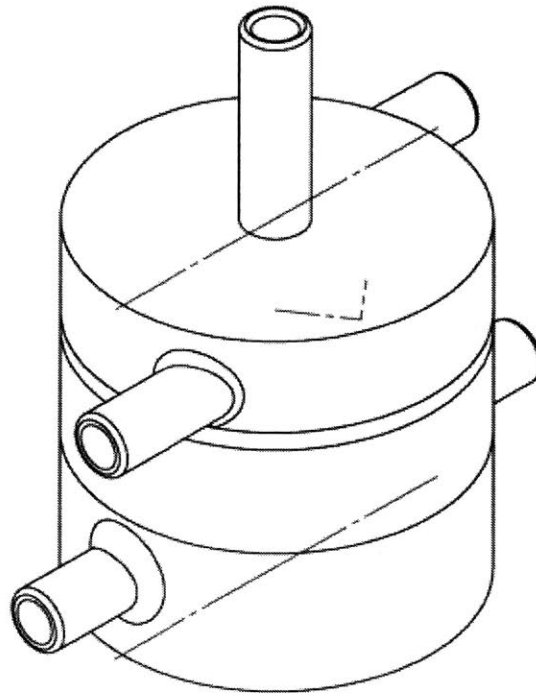
SOLIDWORKS Student Edition.
For Academic Use Only.

(C) KOOLIK AND ROESCH, 2017

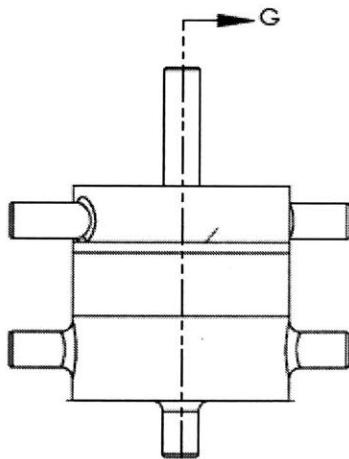
SECTION D-D
SCALE 1 : 1.5

PCVI

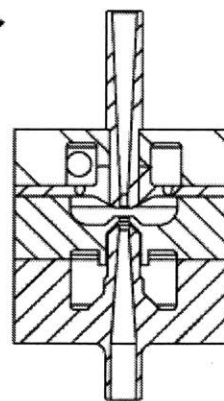
A



B



C



**SOLIDWORKS Student Edition.
For Academic Use Only.**

(C) KOOLIK AND ROESCH, 2017